RSC Advances

Check for updates

Zinc acetate-catalyzed, green and efficient synthesis of xanthene derivatives under ultrasound irradiation: X-ray crystallographic analysis and *in silico* study†

Rayene Sayad,[a] Abdeslem Bouzina,*[a] Yousra Ouafa Bouone,[a] Dounia Beldjezzia,[a] Abdelhak Djemel,[b] Malika Ibrahim-Ouali, [c] Nour-Eddine Aouf[a] and Zineb Aouf [*a]

A simple, one-pot method using zinc acetate and ultrasound irradiation has been developed to synthesize xanthene derivatives from cyclic diketones and aromatic aldehydes, yielding good to excellent results. This method offers advantages like mild conditions, high atom economy, easy isolation, and a recyclable catalyst. All xanthene derivatives, including two new molecules, were confirmed using standard spectroscopic methods, with X-ray crystallographic data provided for compound **3r**. The synthesized molecules were shown to inhibit the VEGFR-2 enzyme, confirmed by molecular docking studies. A 200 ns molecular dynamics simulation validated these findings, showing significant stability for the **3e**-VEGFR-2 complex after 1 ns and the **3p**-VEGFR-2 complex for 8 ns. DFT calculations were used to analyze electronic and geometric properties, including HOMO and LUMO bandgap energies and molecular electrostatic potential surfaces. Additionally, the absorption, distribution, metabolism, and excretion (ADME) properties of the synthesis compounds were assessed.

Introduction

Xanthenes represent a distinct class of tricyclic compounds that incorporate oxygen, and they are encountered in natural products, synthetic bioactive substances, and fluorescent dyes.[1] Xanthene derivatives have garnered considerable attention in the fields of medicinal chemistry and organic synthesis transformations over recent decades.[2] It is noted that many reviews focusing on the synthetic strategies and biological activities of xanthene derivatives have been published.[3–6] These molecules exhibit a range of biological activities, including anti-tumor,[7] anticancer,[8] antibacterial,[9] antiviral,[10] antifungal,[11] analgesic and anti-inflammatory properties.[12] Moreover, owing to their advantageous spectroscopic characteristics, they find applications as dyes in laser technology[13] and fluorescent materials for biomolecule visualization within organisms.[14] Given the substantial interest in xanthene derivatives, a multitude of synthetic protocols has emerged due to their diverse array of

applications. Over the past two decades, various methods and numerous catalysts have been documented for xanthene derivatives synthesis such as CsF,[15] nanoparticles,[16] L-proline,[17] ionic liquid,[18] tetra-*n*-butylammonium fluoride,[19] $CeCl_3 \cdot 7H_2O$,[20] cellulose sulfuric acid,[21] TMSCl,[22] 2-pyridonium hydrogen sulfate,[23] β-CD-BSA,[24] $Co(HSO_4)_2$,[25] $NaHSO_4 \cdot SiO_2$,[26] 2,4,6-tri-chloro-1,3,5-triazine,[27] as well as $SmCl_3$[28] have been employed in these processes. However, many of these methods exhibit various drawbacks, including prolonged reaction times, costly catalysts, harsh conditions, low product yields, and the use of toxic organic solvents.

Recently, $Zn(OAc)_2$ has emerged as a remarkable Lewis acid catalyst for organic synthesis,[29] demonstrating excellent results. In contrast to traditional Lewis acids, $Zn(OAc)_2$ present several advantages, including widespread commercial availability, low price, recyclability, ease of use as an organo-catalyst, environmental friendliness, and a high degree of compatibility with oxygen- and nitrogen-containing substrates and various functional groups.[30]

As part of our ongoing research efforts aimed at pioneering environmentally sustainable methodologies, we report a green and efficient synthesis of xanthene derivatives catalyzed by zinc acetate using ultrasound irradiation, which is a green source of energy for activating chemical reactions.

Further, all synthesized compounds were subjected to *in silico* molecular docking study and molecular dynamics simulation against the vascular endothelial growth factor receptor-2

[a] *Laboratory of Applied Organic Chemistry, Bioorganic Chemistry Group, Sciences Faculty, Chemistry Department, Badji Mokhtar-Annaba University, Box 12, 23000 Annaba, Algeria. E-mail: zineb.aouf@univ-annaba.dz*

[b] *Research Unit in Medicinal Plants, URPM, Attached to Research Center of Biotechnology, CRBt, 3000 Laghouat, 25000 Constantine, Algeria*

[c] *Aix Marseille Univ., CNRS, Marseille F-13397, France*

(VEGFR-2) enzyme to assess their potential for inhibiting it. VEGFR-2 is one of the human enzymes that are considered as interesting targets for drug development of cancer chemotherapy. It plays a crucial role in regulating of tumor angiogenesis with VEGFR-2-related kinases considering as the principal transducers of VEGF-dependent angiogenesis. Consequently, the inhibition of the VEGF/VEGFR signalling pathway is deemed a promising therapeutic strategy for impeding tumor angiogenesis and subsequent tumor growth.[31]

Furthermore, we conducted a comprehensive investigation of the chemical reactivity of the studied compounds using DFT calculations. Additionally, ADME analyses were carried out to evaluate the physicochemical properties and performance of the tested compounds.

Results and discussion

Chemistry

In recent years, the combination of sonochemistry with catalytic systems has become a powerful strategy that integrates the advantages of ultrasound and catalysis to enhance chemical reactions. This synergistic approach has demonstrated significant benefits in various fields, including organic synthesis, pharmaceuticals industries, environmental chemistry, and materials sciences.[32] This combined system provides advantages that include reduced reaction duration, improved heat and mass transfer, resulting in increased chemical reaction rates, yields, and selectivity.[33]

In this context, several methodologies have been documented for the synthesis of xanthene compounds from dimedone and aldehydes, using a combination of sonochemistry and catalytic system under various reaction conditions. Table 1 provides a summary of selected studies described in the literature.

Based on previous research, our objective in this study was to develop an innovative method for the synthesis of xanthene derivatives using Zn(OAc)$_2$/ultrasonic irradiation as a combined system. To facilitate the optimization of the model reaction, we selected dimedone (**1a**) and benzaldehyde (**2a**) as model reactants while subjecting then to ultrasonic irradiation. We then investigated the influence of Zn(OAc)$_2$ under various reaction conditions (Scheme 1 and Table 2).
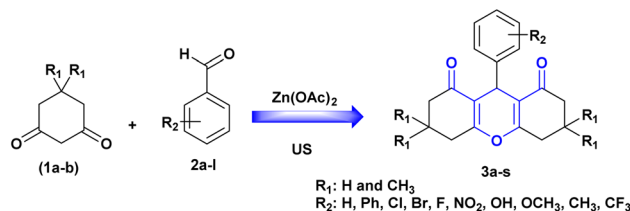
Scheme 1 Zn(OAc)$_2$/US as a combined system for the preparation of xanthene derivatives.

Based on previous research, our objective in this study was to develop an innovative method for the synthesis of xanthene derivatives using Zn(OAc)$_2$/ultrasonic irradiation as a combined system.

To facilitate the optimization of the model reaction, we selected dimedone (**1a**) and benzaldehyde (**2a**) as model reactants while subjecting then to ultrasonic irradiation. We then investigated the influence of Zn(OAc)$_2$ under various reaction conditions (Scheme 1 and Table 2).

Initially, the reaction was performed in catalyst and solvent free conditions, with the application of ultrasound irradiation (40 kHz) at room temperature. A trace yield of the desired product (**3a**) was attained after long reaction time (entry 1, Table 2). These adverse outcomes encouraged us to employ a commercially accessible, inexpensive and environmentally friendly catalyst such as zinc acetate Zn(OAc)$_2$. For this reason, various concentrations of zinc acetate, specifically at 2, 5, 10, and 15 mol% (entry 2–5, Table 2) were tested in our study. The results showed that the reaction was less efficient when the catalyst was used at a concentration of 2 or 5 mol%, even though the reaction was subjected for a longer time. Simultaneously, when the catalyst concentration was set at 10 or 15 mol%, a good product yield was achieved. Thus, the utilization of 10 mol% of Zn(OAc)$_2$ proves adequate to promote the reaction. Then, to evaluate the influence of the solvent, several solvents such as dichloromethane, tetrahydrofuran, toluene, acetonitrile, water and ethanol were applied for the model reaction (entry 6–11, Table 2), the desired product (**3a**) was produced with yields ranging from (70–87%) after 30 min. As evidenced in Table 2, ethanol proved to be the most effective solvent for the reaction, with the highest yield of product (**3a**).

Table 1 Literature methods used sonochemical-catalytic systems for the synthesis of xanthene derivatives

No.	Catalysts	Conditions[a]	Times (min)/yields (%)
1	Ceric(IV) ammonium nitrate CAN (5 mol%)	US (40 kHz), 50 °C, isopropanol (2 mL)	35/98 (ref. 34)
2	MCM-41-SO$_3$H (5 mol%)	US (25 kHz), 60 °C, water (5 mL)	60/95 (ref. 35)
3	TiO$_2$ (5 mol%)	US (50 kHz), r.t., ACN (2 mL)	6/90 (ref. 36)
4	Melamine trisulfonic acid MSTA (7.5 mol%)	US (34–37 kHz), 60 °C, ethyl acetate (3 mL)	110/86 (ref. 37)
5	2-Pyrodidonium hydrogen sulfate [H-NMP]$^+$[HSO$_4$]$^-$ (20 mol%)	US (20 kHz), 60 °C, water (20 mL)	50/86 (ref. 38)
6	1-Carboxymethyl-3-methylimidazolium tetrafluoroborate [cmmim][BF$_4$] (200 mg)	US (50 kHz), 30 °C, methanol (1 mL)	50/87 (ref. 39)
7	**Zinc acetate Zn(OAc)$_2$ (10 mol%)**	**US (40 kHz), 60 °C, EtOH (2 mL)**	**15/95 (our work)**

[a] All reactions was achieved with benzaldehyde and dimedone (mole rate 1 : 2).

Table 2 Optimization reaction conditions of benzaldehyde and dimedone

Entry	Catalyst (mol%)	Solvents	Conditions[a]	Times (min)/yields[b] (%)
1	Catalyst-free	Neat	US (40 kHz), r.t.	240/trace
2	Zn(OAc)$_2$ (2 mol%)	Neat	US (40 kHz), r.t.	120/25
3	Zn(OAc)$_2$ (5 mol%)	Neat	US (40 kHz), r.t.	120/50
4	Zn(OAc)$_2$ (10 mol%)	Neat	US (40 kHz), r.t.	120/69
5	Zn(OAc)$_2$ (15 mol%)	Neat	US (40 kHz), r.t.	120/69
6	Zn(OAc)$_2$ (10 mol%)	DCM (2 mL)	US (40 kHz), r.t.	30/78
7	Zn(OAc)$_2$ (10 mol%)	THF (2 mL)	US (40 kHz), r.t.	30/71
8	Zn(OAc)$_2$ (10 mol%)	Toluene (2 mL)	US (40 kHz), r.t.	30/74
9	Zn(OAc)$_2$ (10 mol%)	ACN (2 mL)	US (40 kHz), r.t.	30/70
10	Zn(OAc)$_2$ (10 mol%)	Water (2 mL)	US (40 kHz), r.t.	30/82
11	Zn(OAc)$_2$ (10 mol%)	EtOH (2 mL)	US (40 kHz), r.t.	30/87
12	Zn(OAc)$_2$ (10 mol%)	EtOH (2 mL)	US (40 kHz), 40 °C	15/90
13	**Zn(OAc)$_2$ (10 mol%)**	**EtOH (2 mL)**	**US (40 kHz), 60 °C**	**15/95**
14	Zn (OAc)$_2$ (10 mol%)	EtOH (2 mL)	Without US (agitation, r.t.)	120/trace
15	Zn(OAc)$_2$ (10 mol%)	EtOH (2 mL)	Without US (agitation, reflux)	120/35
16	Zn(OTf)$_2$ (10 mol%)	EtOH (2 mL)	Without US (agitation, r.t.)	120/trace
17	Zn(OTf)$_2$ (10 mol%)	EtOH (2 mL)	US (40 kHz), 60 °C	120/15

[a] Reaction conditions: dimedone (2 equiv.), benzaldehyde (1 equiv.). [b] Isolated yields: the yields were calculated after recrystallization in diethyl ether/*n*-hexane in (6 : 4).

Additionally, we explored the impact of temperature variation by employing different temperature settings in this reaction (entry 12 and 13, Table 2). The highest yield, reaching 95%, was achieved at 60 °C in 15 minutes under ultrasound irradiation, representing an improvement in yield compared to the use of 40 °C and room temperature.

Finally, to demonstrate the influence of ultrasonic irradiation in this reaction, we examined the synthesis of (3a) in the presence of 10 mol% Zn(OAc)$_2$ in ethanol without employing ultrasonic irradiation, both at room temperature and under reflux conditions (entry 14 and 15, Table 2). In the absence of sonication, the formation of product (3a) at 60 °C resulted in a low yield (35%), and at room temperature, the reaction did not progress. Based on these findings, ultrasound irradiation emerges as a promising approach to enhance the synthesis of the xanthene derivatives under conditions previously reported. To investigate the efficiency and versatility of Zn(OAc)$_2$/ultrasound as a combined system for the synthesis of 1,8-dioxo-octahydroxanthenes derivatives. Numerous aromatic aldehydes with different substituents, were subjected with dimedone or 1,3-cyclohexanedione in the optimal reaction conditions to produce the desired products (3a–3t) in excellent yields (95–84%) between (15–45 min), the resulting products are outlined in Table 3.

To investigate the influence of the catalytic anion, the acetate ion, we synthesized xanthene using a zinc precursor catalyst under similar reaction conditions, both with and without ultrasound irradiation. Initially, we attempted the reaction without ultrasound irradiation using zinc triflate as the catalyst at room temperature (entry 16, Table 2), but no product was observed after 2 hours. We then repeated the procedure with ultrasound irradiation and zinc triflate in ethanol (entry 17, Table 2), which produced a small amount of the desired compound within 2 hours, likely due to residual starting material in the reaction mixture. The reaction progress was monitored using thin-layer chromatography (TLC) on silica gel plates with a dichloromethane/methanol (9 : 1) eluent.

Notably, when comparing zinc triflate with zinc acetate under similar reaction conditions, we identified two major drawbacks. Firstly, zinc triflate acts as a homogeneous catalyst dissolved in ethanol, while zinc acetate is a heterogeneous catalyst that can be easily recovered by filtration. Moreover, the use of zinc acetate is more cost-effective compared to zinc triflate (in terms of time, purification methods, and yields).
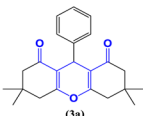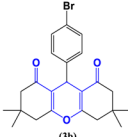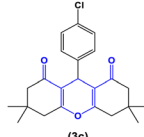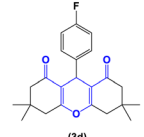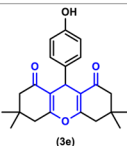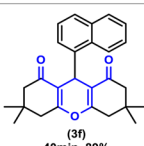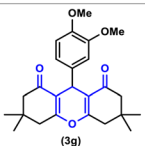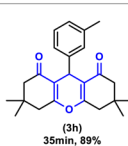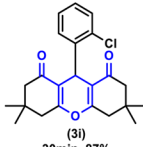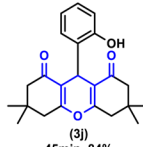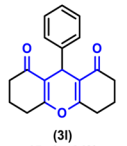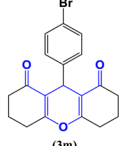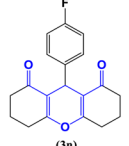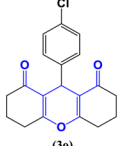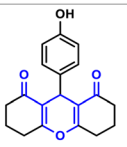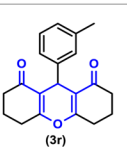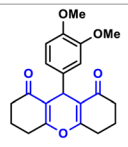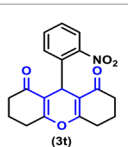
As illustrated in this table, electron-withdrawing and electron-donating substituents on the aromatic ring of aldehydes can partially influence reaction times and yields. Aldehydes with electron-withdrawing groups produce the highest yields (94–90%) in the shortest amount of time (20–25 min), compared to aldehydes with electron-donating substituents. Additionally, substituted aldehydes in *para* positions were found to be more reactive than the *ortho* and *meta* positions. The highest yield (95%) was obtained with benzaldehyde (3a) in 15 minutes, while the lowest yield (84%) was obtained with 2-hydroxybenzaldehyde (3j) in 45 minutes.

Furthermore, compounds 3e, 3j and 3p bearing hydroxyl groups did not react with zinc acetate due to the delocalization of the free electron pairs of the hydroxyl groups, which participate in the mesomerism of the aromatic nuclei, weakening their reactivity. Consequently, we obtain only one product, that of condensation, characterized by usual spectroscopic methods.

The usual spectroscopic methods, including IR and NMR (^{1}H, ^{13}C), were employed to confirm the structures of all the compounds. The IR spectra of compounds (3a–3t) showed absorption bands at 1665 ± 30 cm^{-1} and 1450 ± 30 cm^{-1}, which are attributed to C=O 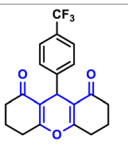and C=C stretching vibrations, respectively. The CH proton signal (between two dimedone or 1,3-cyclohexanedione) of all compounds appeared as a singlet in the ^{1}H NMR spectrum, in the range of 4.80–4.20 ppm. In the ^{13}C NMR spectrum, the carbon situated at the bridge between two

Table 3 Zn(OAc)$_2$/US system for the synthesis of 1,8-dioxo-octahydroxanthene derivatives[a]

(3a) 15min, 95%   (3b) 20min, 93%   (3c) 20min, 94%   (3d) 20min, 92%

(3e) 35min, 88%   (3f) 40min, 89%   (3g) 40min, 86%   (3h) 35min, 89%

(3i) 30min, 87%   (3j) 45min, 84%   (3k) 40min, 85%

(3l) 15min, 94%   (3m) 20min, 91%   (3n) 20min, 92%   (3o) 25min, 93%

(3p) 25min, 89%   (3q) 25min, 90%   (3r) 25min, 87%   (3s) 30min, 85%   (3t) 35min, 90%

[a] Reaction conditions: dimedone or 1,3-cyclohexanedione (2 equiv.), aldehydes (1 equiv.); the yields were calculated after recrystallization in diethyl ether/n-hexane in (6 : 4).

dimedone or cyclohexanedione rings exhibits a chemical shift at ∼50.6 ppm and the carbonyl carbon appears approximately at ∼196.3 ppm.

Zinc acetate can act as a mild Lewis acid, coordinating with the carbonyl oxygen of aldehydes. This increases the carbonyl carbon's electrophilicity to some extent, facilitating nucleophilic attack. While less common than stronger Lewis acids for direct activation, zinc acetate finds use in specific reactions due to its advantageous properties like chemoselectivity. The versatility of zinc acetate is illustrated by the numerous reviews dedicated to its applications in organic synthesis and catalysis.[40]

A plausible mechanism for the synthesis of xanthene derivatives using Zn(OAc)$_2$ has been shown in Scheme 2. Firstly, ultrasound cavitation activates the coordination of Zn(OAc)$_2$ with aldehydes, generating the zinc oxide-aldehydes intermediate (**A**), which then reacts with dimedone/1,3-cyclohexanedione to form intermediate (**B**) after dehydration and removal of Zn(OAc)$_2$. Afterward, the active methylene group of the second molecule of dimedone/1,3-cyclohexanedione reacted with intermediate (**B**) through a conjugate Michael addition, forming intermediate (**C**). This intermediate then underwent intermolecular cyclization with (H$_2$O, Zn(OAc)$_2$ elimination, resulting in the formation of the final products (**D**).

X-ray study

Suitable crystals of compound **3r** were obtained after crystallization in diethyl ether/n-hexane and were exposed to X-ray diffraction analysis in order to completely reveal its structural composition.
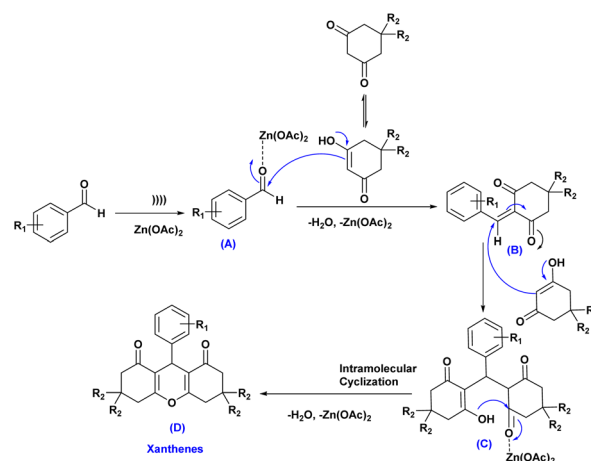
Scheme 2 Proposed mechanism for the synthesis of xanthene derivatives.

Fig. 1   ORTEP diagram of compound **3r**.

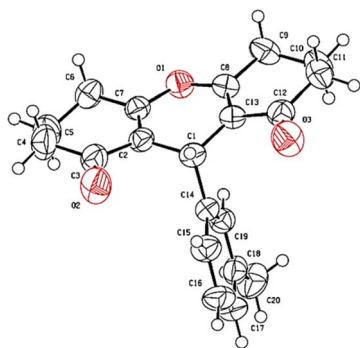As displayed in the ORTEP diagram represented in Fig. 1, the asymmetric unit of the crystal structure comprises one molecule of compound 3,3,6,6-tetramethyl-9-(*m*-tolyl)-3,4,5,6,7,9-hexahydro-1*H*-xanthene-1,8(2*H*)-dione that crystallizes in the orthorhombic system with the *Pca*2_1 space group.

No conventional hydrogen bonds were observed since there is no hydrogen linked to an electronegative heteroatom. However, many short contacts were noticed (Table 4) in the structure that contribute to the linkage of the crystal components including intermolecular contacts of type C–H...O with lengths comprised between 2.609 and 2.654 Å, and C–H...C with a length of 2.847 Å. A crystal-packing diagram was built using Mercury software (Fig. 2), which shows a general view of the repartition of the molecules that constitutes the crystal structure.

A general comparison between the structure of compound **3r** and some previously reported xanthene derivatives differentiated by substituents in various positions indicates resemblances in geometry, bond lengths, and angle values.[41] The bond lengths in the structure closely match those of analogous cyclohexanedione and dimedone-based xanthene compounds. For instance, carbonyl bonds lengths of cyclohexenone ring C3–O2 and C12–O3 are respectively equal to 1.225 and 1.211 Å, which is consistent with previous studies that state a length for carbonyl bond within the range of (1.221–1.229 Å). Similarly, C–O bonds lengths of the central pyranic heterocycle in compound **3r** citing C7–O1 (1.380 Å) and C8–O1 (1.376 Å) align with literature values ranging from 1.376 to 1.380 Å. Cyclohexenone rings adopt half-chair conformations in which C5 and C10 deviated from the planes A and C with distances equal to 0.631 and 0.643 Å respectively. While the pyranic ring displays an almost planar geometry, with atom C1 distancing from the plane B by a length of 0.287 Å (Fig. 3). These findings are in
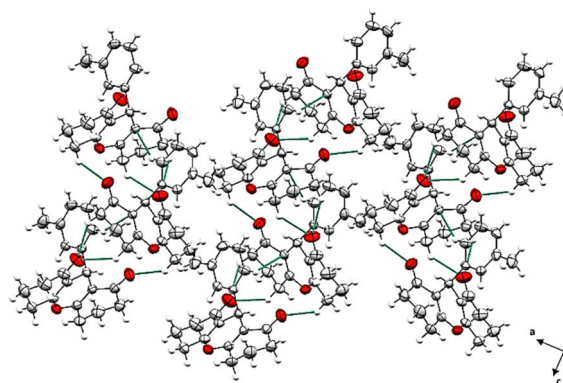
Fig. 2   Crystal packing diagram viewed along (*b*) axis represented as ellipsoids drawn at 40% probability level. Contacts are represented as green dashed sticks.

perfect reliability with crystallographic identifications of similar xanthenedione rings.[42] Furthermore, torsions angles compared to the aromatic ring are near to 180°, which suggests an antiperiplanar conformation.

In silico study

Molecular docking. VEGFR-2 is a prominent subject of study in molecular docking research, particularly in the field of drug discovery and development. This receptor plays a crucial role in regulating angiogenesis and the process of forming new blood vessels from existing ones. Understanding the molecular interactions involving VEGFR-2 is of immense importance because it offers the potential to develop novel therapeutic interventions for various medical conditions, with a strong emphasis on cancer and disorders linked to abnormal angiogenesis.[43]

The field of molecular docking, when applied to VEGFR-2, focuses on how small molecules, often potential drug candidates, interact with this receptor at the atomic and molecular level. By employing advanced computational methods and docking software, researchers can predict and evaluate the binding affinity and structural interactions between VEGFR-2 and these molecules. This provides valuable insights into the potential efficacy of compounds in modulating the receptor's activity.

Molecular docking studies involving VEGFR-2 also can help researchers identify and prioritize compounds that can selectively target VEGFR-2, either by inhibiting or activating its signalling pathways. This selectivity is vital because it allows for

Table 4   Short contacts in the crystal structure of compound **3r**

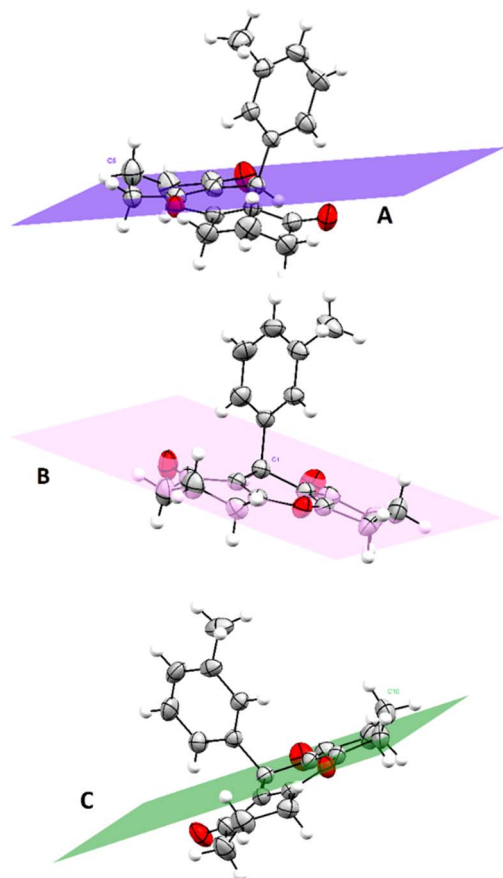| D–H...A	d(D–H)	d(H...A)	d(D–A)	D–H–A	Symmetry
C9–H9A...O2	0.970	2.613	3.416(5)	140.2	*x*, *y*, *z*; 1 − *x*, 1 − *y*, −1/2 + *z*
C11–H11B...O2	0.970	2.654	3.488(5)	144.3	*x*, *y*, *z*; 1 − *x*, 1 − *y*, −1/2 + *z*
C6–H6B...O3	0.970	2.609	3.432(4)	142.8	*x*, *y*, *z*; 1 − *x*, 1 − *y*, −1/2 + *z*
C15–H15...C13	0.930	2.847	3.702(4)	153.2	*x*, *y*, *z*; 1 − *x*, 1 − *y*, −1/2 + *z*

Fig. 3 Graphical representation of planes A, C corresponding to cyclohexenones rings and plane B corresponding to the pyranic cycle. (Plane A: calculated through C2–C3–C4–C6–C7, plane B: calculated through C2–C7–O1–C8–C13, and plane C: calculated through C8–C9–C11–C12–C13). Obtain permission and include the acknowledgement required by the copyright holder if a figure is being reproduced from another source.

the development of precise, targeted therapies with reduced off target effects and minimal harm to healthy tissues.

Furthermore, the insights gained from molecular docking studies can guide the design and optimization of potential drug candidates, ensuring their maximum efficacy and safety. VEGFR-2, as a key player in angiogenesis regulation, is a focal point for molecular docking investigations. These studies offer a gateway to the development of tailored therapies for cancer and angiogenesis-related disorders, potentially improving patient outcomes and the quality of medical treatments.

In order to gain a comprehensive understanding of the interactions between the active site of VEGFR-2 and ligands, we conducted molecular docking study to explore the binding modes of compounds under investigation. Our studies were performed using Schrodinger Suite (version 11.8) and Chimera X programs. We utilized 4-amino-furo[2,3-d] pyrimidine as the reference ligand to investigate the binding mode. The accuracy of the docking protocol was assessed through the re-docking of the reference ligand into the active site of VEGFR-2. Fig. 4 illustrates the docked reference ligand and the co-crystallized
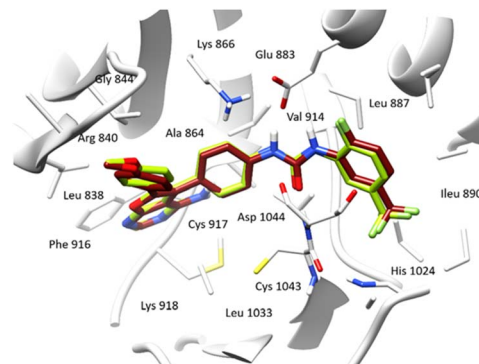

Fig. 4 Docked and co-crystalized 4-amino-furo[2,3-d] pyrimidine in the active site of VEGFR-2 enzyme after self-docking calculation. (Co-crystallized ligand in green sticks and the docked ligand in brown sticks).

one occupying almost the same position within the receptor (RMSD = 0.38 Å). This confirms the validation of our docking protocol, which utilized the standard precision (SP) scoring function, in absence of water molecules.

The results of this study, including the estimated glide score of the docked positions, are provided in Table 5 and Fig. 5. Our molecular docking analysis of all studied compounds revealed that the majority of the compounds exhibit a good stability within the binding cavity. Specifically, compounds **3t, 3p, 3e, 3i, 3b, 3m** and **3c** displayed superior glide scores compared to the other when binding to the target protein.

These compounds exhibited an average binding score ranging from -6.99 to -6.12 kcal mol^{-1}. On the other hand, compounds **3f, 3a** and **3o** demonstrated lower stability compared to the rest, with glide score of -4.80, -5.08 and

Table 5 Docking score (kcal mol^{-1}) of synthesized xanthene derivatives (**3a–3t**) and the reference ligand (4-amino-furo[2,3-d] pyrimidine) against VEGFR-2 enzyme by molecular docking study

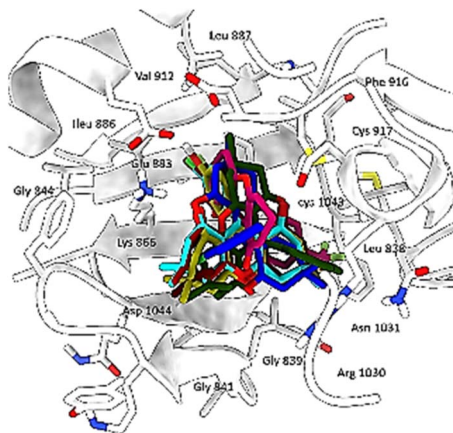| Compound code	Docking score
3a	-5.08
3b	-6.24
3c	-6.12
3d	-6.02
3e	-6.52
3f	-4.80
3g	-6.01
3h	-5.28
3i	-6.34
3j	-5.80
3k	-5.12
3l	-6.10
3m	-6.20
3n	-5.94
3o	-5.20
3p	-6.80
3q	-5.80
3r	-6.05
3s	-5.40
3t	-6.99
Reference ligand	-13.11

Fig. 5 Superimposition of the most stable xanthene derivatives in the active site of VEGFR-2 enzyme.

-5.20 kcal mol^{-1}, respectively. These findings provide valuable insights into the binding affinity of these compounds with the target protein.

A thorough analysis of the molecular docking results revealed that hydrogen bonds, hydrophobic forces, and electrostatic attractions primarily drove the interactions within the active site of the VEGFR-2 enzyme.

The obtained results play a crucial role in determining the binding affinity and specificity of molecules within the enzyme's binding pocket, shedding light on the potential effectiveness of various ligands in modulating VEGFR-2 activity. The docking outcomes for the xanthene compounds, as well as the reference ligand, have been presented in Table 6.

The reference ligand exhibits outstanding stability within the active pocket, as indicated by a docking score of -13.11 kcal mol^{-1}, owing to the presence of functional groups in its structure. These functional groups are capable of forming four crucial hydrogen bonds with Glu883, Cys917, Glu915 and Asp1044 residues, which play a significant role in inhibiting the VEGFR-2 enzyme. Additionally, the reference ligand engages in hydrophobic interactions with several residues, including Phe 916, Leu 383, and Cys 1043, creating strong attractions with the aromatic rings of the reference ligand (Fig. 6).

Both compounds **3e** and **3p** exhibited notable stability within the active site of the VEGRF-2 enzyme owing to the presence of a hydroxyl group in the *para* position of their aromatic rings, forming a crucial hydrogen bond with the key residue Glu803.

This hydroxyl group significantly enhances the stability of these ligands within the active pocket. Additionally, compound **3e** established an additional hydrogen bond and cation interaction with Lys866, a residue contributing to the enzyme's inhibition (Fig. 7).

Moreover, both compounds displayed significant hydrophobic interactions with residues Phe916, Cys917, Val897, Leu1033, and Cys1043, which are known to play a role in inhibiting the VEGRF-2 enzyme. These interactions elucidate the molecular docking values and contribute to the understanding of the compounds inhibitory mechanisms.

Compound **3s** showed equal significance to compounds **3e** and **3p**, exhibiting considerable stability within the active site with acceptable docking scores. **3s** forms a crucial hydrogen bond with the residue Asp1044, known among the residues responsible for inhibiting the VEGRF-2 enzyme, and an ionic bond with the key residue Glu883. Additionally, it participates in notable hydrophobic interactions, particularly through a π–cation interaction with the residue Lys886.

After analyzing other compounds, we have observed that the nature of the substituent on the phenyl ring significantly influences stability within the active site. Compounds containing a halogen substituent on the aromatic ring or a secondary aromatic ring, such as in the case of a naphthalene group, exhibit average stability compared to other compounds within the pocket. Compound **3f** exemplifies this characteristic.

Structure–activity relationship (SAR). Structure–activity relationship (SAR) studies have focused on molecules analogous to the xanthene skeleton, where the aromatic rings have been replaced by unsaturated aliphatic rings, either unsubstituted or substituted with four methyl groups (dimedone derivatives). Numerous FDA-approved drugs feature the xanthene pharmacophore,[44] as well as extensive literature documenting the anticancer and antitumor activities of the xanthene skeleton.[45] Many of these compounds exhibit potent inhibition against cancer cells.

In our investigation, we employed *in silico* studies to analyze the interaction of our compounds with the VEGFR-2 enzyme, a known cancer target, aiming to elucidate their inhibitory mechanisms. The xanthene pharmacophore, comprised of three rings, served as the basis for our modifications, primarily focused on substituents on the aromatic ring.

The base molecule **3a**, which does not carry any electron-donating or electron-withdrawing substituents at the aromatic ring level, presented an inhibition of the VEGFR-2 enzyme with an average docking score of -5.08 kcal mol^{-1}. This is due to the fact that the ligand **3a** does not form hydrogen bonds with key active site residues. On the other hand, the introduction of substituents such as fluorine, chlorine, methoxy, hydroxy, and others confers several advantages, particularly enhancing inhibitory potency. These derivatives also share the common xanthene pharmacophore, which is intricately linked to a ring system. Notably, the positions and types of substituents on the aromatic ring exert a significant influence on the outcomes of molecular docking studies.

Our findings indicate that the incorporation of a hydroxyl substituent at the *para* position of the aromatic ring in compounds **3e** (-6.52 kcal mol^{-1}) and **3p** (-6.80 kcal mol^{-1}) demonstrates significant *in silico* inhibition of the VEGFR-2 enzyme due to the formation of hydrogen bonds with key active site residues. Additionally, electron-withdrawing groups, such as the methoxy group and halogens like fluorine, chlorine, and bromine at the *para* position, also exhibit notable inhibition.

Conversely, groups such as nitro, methyl, and methoxy show comparatively lesser inhibition. Furthermore, substituents at position *ortho* of the aromatic ring interfere with molecular

Table 6 Analysis of binding interaction of xanthene derivatives **3a–3t** with the reference compound against VEGFR-2 enzyme

Code	Hydrogen bond	Hydrophobic interaction	Pi-cation
3a	—	Val897, Cys1043, Ala864, Val846, Val914, Phe916, Cys917, Leu838, Leu1033	—
3b	Lys866	Val846, Phe843, Leu838, Leu1033, Cys917, Phe916, Val914, Val912, Leu887, Ala864, Val865	Lys866
3c	Lys866	Val846, Leu838, Leu1033, Cys917, Phe916, Cys1043, Val897, Val914, Val912, Leu887, Ala864, Val865	Lys866
3d	Lys866	Val846, Phe843, Leu838, Leu1033, Cys917, Phe916, Val914, Val912, Val897, Leu887, Ala864	Lys866
3e	Lys866, Glu883	Val846, Phe843, Leu838, Leu1033, Cys917, Phe916, Val914, Val912, Leu887, Cys1043, Ala864	Lys866
3f	—	Val846, Leu838, Leu1033, Cys917, Phe916, Val914, Val897, Leu887, Cys1043, Ala864	—
3g	Lys866	Ala864, Val897, Val914, Leu1033, Cys1043, Val846, Phe843, Ala842	Lys866
3h	—	Val897, Cys1043, Ala864, Val914, Phe916, Cys917, Leu838, Leu1033, Val846	—
3i	Lys866	Val846, Leu838, Leu1033, Cys917, Phe916, Val914, Cys1043, Val897, Ala864, Leu887	—
3j	Leu838	Val846, Ala864, Val914, Phe916, Cys917, Leu838, Leu1033, Cys1043, Val897	—
3k		Leu887, Cys1043, Val914, Val912, Val265, Val897, Phe916, Cys917, Ala864, Leu1033, Leu818, Val846	
3l	—	Leu887, Cys1043, Val914, Val912, Val265, Val897, Phe916, Cys917, Ala864, Leu1033, Leu818, Val846	—
3m	—	Leu887, Cys1043, Val914, Val912, Val265, Val897, Phe916, Cys917, Ala864, Leu1033, Leu818, Val846	—
3n	—	Val846, Leu838, Cys917, Phe916, Val914, Val912, Leu1033, Val897, Cys1043, Leu887, Val865, Ala864	Lys866
3o	—	Val846, Leu838, Cys917, Phe916, Val914, Val912, Val897, Cys1043, Leu1033, Leu887, Ala864, Val865	—
3p	Glu883	Val846, Leu838, Val914, Phe916, Cys917, Val897, Leu1033, Cys1043, Ala864, Leu887	—
3q	—	Val914, Phe916, Cys917, Ala864, Val846, Leu838, Leu1033, Cys1043, Val897, Leu887	—
3r	—	Val846, Leu838, Cys917, Phe916, Val914, Ile913, Val912, Leu1033, Val897, Cys1043, Val865, Ala864	—
3s	Cys917	Val846, Leu838, Val914, Phe916, Cys917, Val897, Leu1033, Cys1043, Ala864, Leu887	Lys866
3t	—	Val846, Leu838, Val914, Phe916, Cys917, Val897, Leu1033, Cys1043, Ala864, Leu887	—
Ref. ligand	Glu883, Cys917, Glu915, Asp1044	Ile896, Leu887, Ile890, Leu1017, Ile1042, Cys1043, Val896, Val897, Val914, Phe916, Cys917, Ala864, Leu1033, Leu838, Val846	—

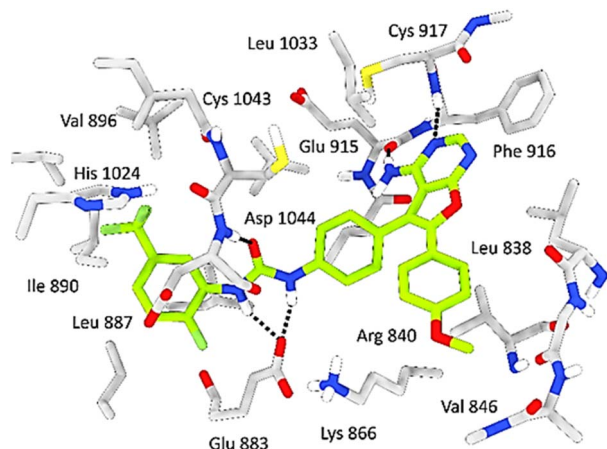© 2024 The Author(s). Published by the Royal Society of Chemistry

Fig. 6 3D binding interactions of the reference ligand after docking calculations in the active site of VEGFR-2 enzyme. The amino acid residues were shown as grey stick model and H-bonds were shown as black lines.

stabilization within the active pocket, consequently diminishing enzyme inhibition.

Molecular dynamics simulation. Molecular dynamics studies simplify the identification of protein regions affected by a ligand inside the physiological environment. These methods explicitly account for the flexibility of the entire protein–ligand system, enabling validation of docking poses.[46] Therefore, our

study aimed to confirm the previously predicted binding mode of compounds **3e** and **3p** within the active site of the VEGFR-2 enzyme.

Our investigation involved assessing system stability through variations in RMSD values, the count of hydrogen bonds between the selected ligands and VEGFR-2 enzyme and the protein–ligand contacts analysis. The other parameters such as the root mean square fluctuation (RMSF), the radius of gyration and DSSP, and monitoring the protein secondary structure elements (SSE) like alpha helices and beta-strands throughout the simulation will be presented in the ESI.†

Root mean square deviation (RMSD). Root Mean Square Deviation (RMSD) is a statistical measure used to quantify the average distance between the atoms of two superimposed structures. It calculates the square root of the average of the squared differences between the positions of equivalent atoms.

Specifically in biology, the predictive assessment of the gap between the ligand and the protein relies on evaluating PL-RMSD (Protein and Ligand Root Mean Square Deviation) extracted from MD simulation trajectories. Deviations falling within the 1 to 3 Å range are supposed acceptable for small molecules. PL-RMSD serves as a metric to measure the distance fluctuations between the protein and its associated ligand across the simulation duration. Initially, all 1000 protein frames are aligned to the reference frame backbone (frame 0), following which the RMSD is computed based on C-Alpha atoms.
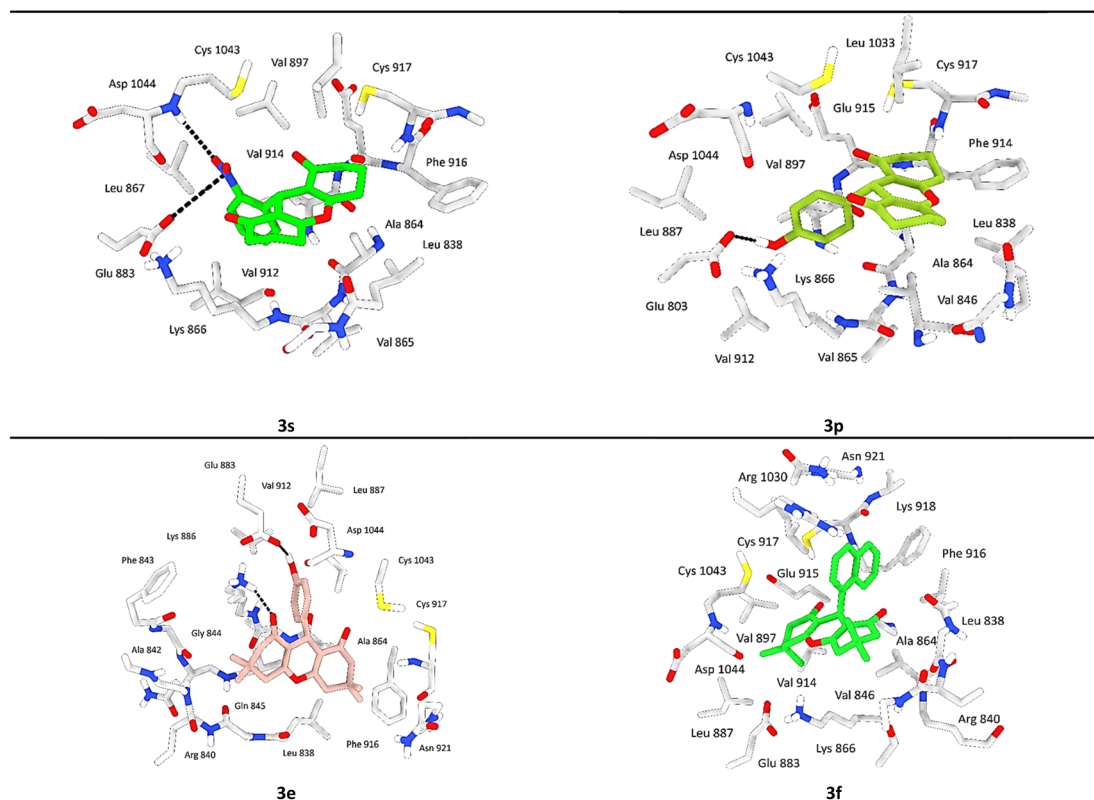

Fig. 7 3D binding interactions of compounds **3s**, **3p**, **3e** and **3f** after docking calculations in the active site of VEGFR-2 enzyme. The amino acid residues were shown as grey stick model and H-bonds were shown as black lines.

Continuous monitoring of protein RMSD offers insights into structural variations throughout the simulation, shedding light on whether the simulation maintains equilibrium and whether its fluctuations revolve around a certain thermal average. Notably, higher RMSD values suggest potential instability within the protein system.

The comparative RMSD analysis between the VEGFR-2 protein and ligand **3e** bound indicates consistent values for both structures from the onset of the MD simulation. It is notable that equilibrium was achieved by all systems after 1 ns (Fig. 8). Subsequently, we divided our productive phase into time intervals ranging from 1 to 200 ns across all simulations. Beyond the initial 1 ns of MD simulation, the observed ligand-RMSD values closely mirrored those of the protein's RMSD, implying a strong and sustained stability between ligand **3e** and the protein within its binding pocket.

Furthermore, an examination of the PL-RMSD values underscores continuous backbone stability throughout the MD simulation while ligand **3e** remains bound to the protein. Typically, if the observed values significantly exceed the RMSD of the protein, it suggests that the ligand may have diffused away from its initial binding site. However, in the case of ligand **3e**, minimal variance (ranging from 1.0 to 2.0 Å) is observed between the protein and ligand RMSD, indicating that the ligand remains proximate to its original position throughout the 200 ns of simulation time.

For the ligand **3p**, substantial stability was observed after 8 ns of MD simulation, marking the start of the productive phase divided into time intervals spanning from 8 to 200 ns across all simulations (Fig. 8). This stability is clearly evidenced by the ligand-RMSD values closely aligning with the RMSD of the protein, indicative of a consistent and robust interaction between the **3p** ligand and the protein within its binding pocket. Such alignment suggests a persistent and favorable binding mode.

During the productive phase, minimal variance (ranging from 0 to 0.6 Å) was observed between the protein and ligand RMSD, underscoring that the **3p** ligand remains in close proximity to its original position throughout the 200 ns of simulation time.

Protein–ligand contacts analysis. The analysis of VEGFR-2 enzyme and its interactions with **3e** and **3p** ligands revealed three distinct types of interactions: hydrogen bonds, hydrophobic interactions, and water bridges.

Hydrogen bonds play a crucial role in the binding of ligands to protein residues. Thus, considering the properties of hydrogen bonding is essential in drug design due to their significant impact on drug specificity, metabolism, and adsorption. In our study, we present the hydrogen bonds formed between the studied ligands and the VEGFR-2 enzyme during the 200 ns of MD simulation, as depicted in Fig. 9.

The results showed that the ligand **3e** can form up to 5 hydrogen bonds on average during the 200 ns of MD simulation with Lys 866, Glu915, Cys917, Cys1043 and Asp1044 residues; and the ligand **3p** can form up to 5 hydrogen bonds with Lys866, Glu883, Asn1031, Cys1043, and Asp1044.

Regarding hydrophobic interactions, which play a key role in stabilizing the ligand–protein complex, they are typically classified into three subtypes: π–cation, π–π stacking, and other non-specific interactions. Typically, these interactions involve a hydrophobic amino acid and either an aromatic or aliphatic group on the compound. The analysis revealed that both compounds **3e** and **3p** exhibit strong bonding interactions within the active site of the VEGFR-2 enzyme. The identification of a π–cation interaction between the ligand **3e** and the Lys 866 residue led us to an explanation of why the ligand **3e** attains a superior docking score compared to the ligand **3p**, which lacks π–cation or π–π stacking interactions.
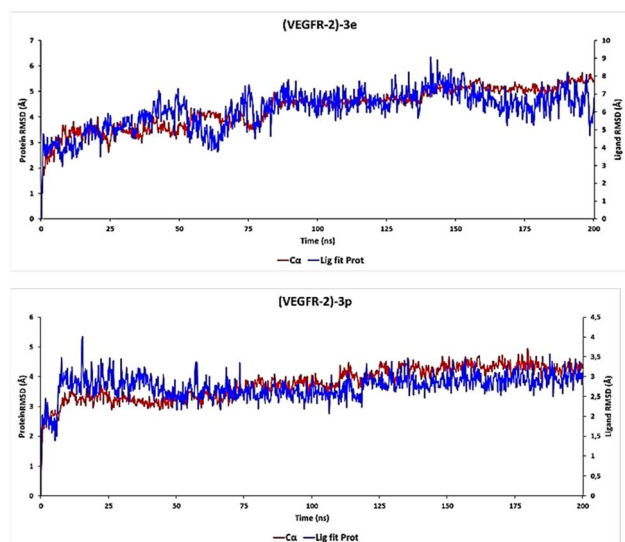

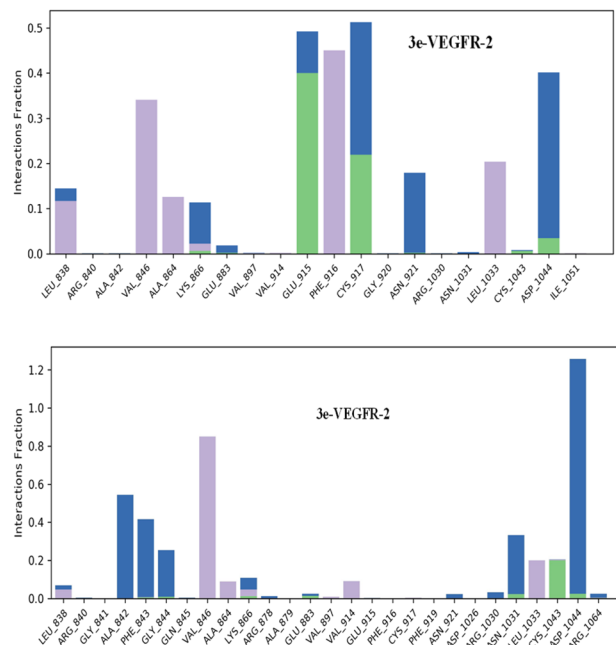Fig. 8 (PL-RMSD) obtained from the MD simulation trajectories (**3e** and **3p**).

Fig. 9 Protein–ligand contacts obtained from the MD simulation trajectories.

Density functional theory. Density functional theory (DFT) is a significant part of computational chemistry and an extensive methodology that aims to calculate molecular properties and define the electronic comportment of a structure in different states. Besides, it is effectively used to assess reactivity and chemical stability.

In completion of our *in silico* study, and in order to associate the predicted binding mode of xanthene derivatives and their structural properties, we conducted a computational investigation through density functional theory (DFT) in which we used the B3LYP/6-31G(d,p) model contained within Gaussian 09 to obtain optimized molecular geometries, determine electron density of compounds, and define their different global chemical reactivity descriptors citing chemical hardness (η), molecular softness (s), electronic chemical potential (μ), electronegativity (χ), and electrophilicity index (ω), results are depicted in Table 7.

Dipole moment that defines charge separation in a molecule and its polarity are included in the range [4.7750–8.1477D] for the studied xanthene-based molecules. Compound **3j** was noted as the most polar and compound **3e** as the least polar among investigated compounds. Optimized molecular geometries as well as frontier molecular orbitals are represented in Fig. 10, HOMO–LUMO energy gaps ranges between 3.6697 and 4.6904 eV in which compound **3q** showed the highest value, hence, it is the most stable compound among xanthene derivatives.

The molecular electrostatic potential (MEP) is an effective tool to predict electron-rich and electron-deficient positions in a structure, and learn more about the behavior of a molecule towards other molecules or biological systems including reactivity and the ability of hydrogen bonds formation. MEP surface of all compounds were determined from DFT structure optimization results using B3LYP method at 6-31G(d,p) level and were visualized as shown in Fig. 10. Every derivative has a color code lying in a specific range between the deepest red and the deepest blue. Red color in the MEP indicates the most nucleophilic (negative) parts of the molecules while the blue color designates the most electrophilic (positive) fragments.

ADME analysis. Combinatorial chemistry and high-throughput screening have significantly expanded the pool of compounds requiring early data on absorption, distribution, metabolism, and excretion (ADME). These parameters are important in the development of new drug molecules as they determine the dosage, dosing interval, and overall safety margins. The molecules' pharmacokinetic characteristics define these safety margins. The drug-likeness of synthesized compounds is predicted by analyzing their ADME properties using the SwissADME server, based on Lipinski's rule of five. These descriptors play a significant or pivotal role in determining a molecule's suitability as a drug: $mi\log P$ (octanol–water partition coefficient) ≤ 5, molecular weight ≤ 500, number of hydrogen bond acceptors ≤ 10, and number of hydrogen bond donors ≤ 5.

In this study, the drug likeness and ADME properties of the investigated compounds were explored, and compared with rhodomyrtone drug. The predicted physico-chemical properties are summarized in Table 8. The molecular weight of rhodomyrtone and the studied compounds (**3a–3t**) ranged from 294.34 to 442.54 g mol^{-1} (<500). Low molecular weight drug

Table 7 Calculated molecular descriptors of the studied xanthene derivatives obtained by DFT B3LYP/6-31G (d,p) method in gas phase[a]

Molecular descriptors (gas phase)

Entry	$\log P$	μ (D)	E_{HOMO} (eV)	E_{LUMO} (eV)	ΔE_{gap}	(η)	(S)	(μ)	(χ)	(ω)
3a	2.08	6.0432	−6.1471	−1.5445	4.6025	2.3013	0.4345	−3.8458	3.8458	3.2135
3b	2.91	7.3494	−6.1416	−1.6936	4.4480	2.2240	0.4496	−3.9176	3.9176	3.4505
3c	2.64	7.4033	−6.2042	−1.6920	4.5122	2.2561	0.4432	−3.9481	3.9481	3.4545
3d	2.24	6.8678	−6.1149	−1.6262	4.4888	2.2444	0.4456	−3.8705	3.8705	3.3375
3e	1.69	4.7750	−5.6145	−1.5124	4.1021	2.0511	0.4876	−3.5635	3.5635	3.0955
3f	3.08	5.7832	−5.5130	−1.5818	3.9312	1.9656	0.5087	−3.5474	3.5474	3.2011
3g	1.83	7.1153	−5.4768	−1.4887	3.9881	1.9941	0.5015	−3.4828	3.4828	3.0415
3h	2.57	5.6706	−6.0861	−1.5233	4.5628	2.2814	0.4383	−3.8047	3.8047	3.1725
3i	2.64	7.1479	−6.1710	−1.6098	4.5612	2.2806	0.4385	−3.8904	3.8904	3.3183
3j	1.69	8.1477	−5.4975	−1.8278	3.6697	1.8349	0.5450	−3.6627	3.6627	3.6556
3k	2.87	9.1839	−6.3639	−1.9323	4.4316	2.2158	0.4513	−4.1481	4.1481	3.8827
3l	0.48	6.0239	−6.1612	−1.5666	4.5946	2.2973	0.4353	−3.8639	3.8639	3.2493
3m	1.31	7.2722	−6.1509	−1.7173	4.4336	2.2168	0.4511	−3.9341	3.9341	3.4909
3n	0.64	6.8094	−6.1272	−1.6490	4.4782	2.2391	0.4466	−3.8881	3.8881	3.3758
3o	1.04	7.3246	−6.2162	−1.7162	4.4999	2.2500	0.4444	−3.9662	3.9662	3.4958
3p	0.09	7.1185	−5.6295	−1.5350	4.0945	2.0472	0.4885	−3.5822	3.5822	3.1341
3q	1.41	7.8681	−6.4736	−1.7832	4.6904	2.3452	0.4264	−4.1284	4.1284	3.6337
3r	0.97	6.1091	−6.0251	−1.5429	4.4823	2.2411	0.4462	−3.7840	3.7840	3.1945
3s	0.23	7.1539	−5.4820	−1.5075	3.9745	1.9872	0.5032	−3.4948	3.4948	3.0729
3t	0.86	9.2091	−6.4031	−1.9497	4.4534	2.2267	0.4491	−4.1764	4.1764	3.9166

[a] Dipole moment (μ), energy of the highest occupied molecular orbital (E_{HOMO}), energy of the lowest unoccupied molecular orbital (E_{LUMO}), the HOMO–LUMO gap (ΔE_{gap}), chemical hardness (η) = ($E_{LUMO} - E_{HOMO}$)/2, molecular softness (S) = $1/\eta$, electronic chemical potential (μ) = $-\chi$ = ($E_{HOMO} + E_{LUMO}$)/2, electronegativity (χ) = $-(E_{HOMO} + E_{LUMO}$)/2, electrophilicity index (ω) = $\mu^2/2\eta$.
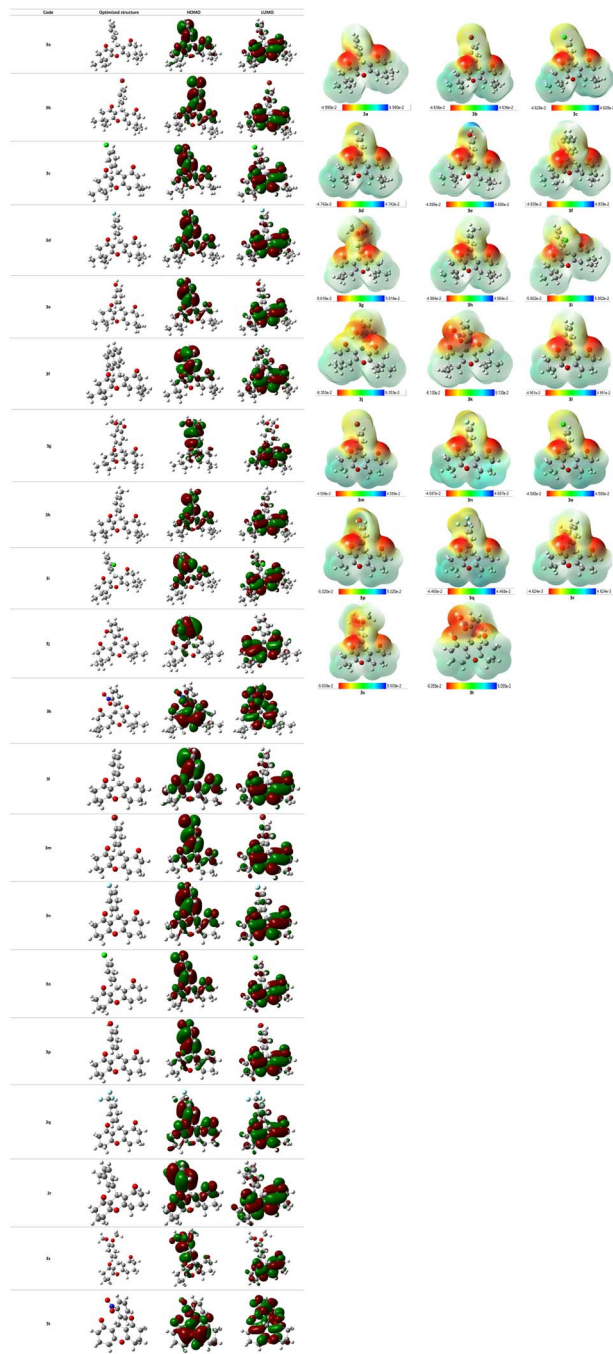
Fig. 10 Representation of HOMO/LUMO orbitals and optimized structures at B3LYP/6-31G(d,p) level in gas phase.

molecules (<500) can be transported, diffused, and absorbed more easily compared to heavier molecules. Molecular weight plays a crucial role in therapeutic drug action; if it increases significantly, it can impact the drug's effectiveness. The number of hydrogen bond acceptors and donors in the tested compounds was found to be within Lipinski's limit. The hydrogen bond acceptor count ranged from 3 to 6 (<10), and the hydrogen bond donor count was less than 5 in all molecules (<5). Additionally, most compounds have one rotatable bond, except for compounds (**3q**, **3k**, and **3t**) which have 2, and

compounds **3g** and **3s**, which have 3 rotatable bonds, respectively (<10). These compounds exhibited favorable lipophilicity, as indicated by their $i \log P$ values ranging from 2.83 to 3.81, which are less than <5.

Furthermore, these compounds demonstrated excellent water solubility, as evidenced by $\log S$ ESOL values ranging from −3.12 to −5.79. A value below −10 is considered insoluble, whereas a value above −4 is considered soluble according to SwissADME solubility measurements ($\log S$). In fact, a soluble molecule simplifies various aspects of drug development, especially handling and formulation. Regarding oral administration, researchers have noted that solubility plays a crucial role in determining absorption.

On the other hand, the skin permeability coefficient (K_p) is linearly related to molecule size and lipophilicity, and $\log K_p$ (cm s^{-1}) measures a molecule's permeability through the skin. A higher value of $\log K_p$ indicates a lower likelihood of the molecules permeating the skin. Among the aforementioned compounds, **3g** exhibited the lowest skin permeability (−6.93 cm s^{-1}), whereas **3l** showed high skin permeability (−4.13 cm s^{-1}). Compounds with high skin permeability are generally less suitable for oral medication. Meanwhile, the topological polar surface area ranged between 43.37 and 89.19 Å^2 compared to the topological polar surface area of the rhodomyrtone drug, which is 100.90 Å^2, all of these values, fell within the recommended ranges for oral bioavailability.

Dynamic Lipophilicity (DLS) is a parameter that assesses how well a compound aligns with the characteristics of drug molecules. Interestingly, compound **3s** exhibited the highest DLS value of 0.07 even better than rhodomyrtone drug (DLS = −0.33), consistent with experimental bioactivity results. In contrast, compound **3a** displayed the lowest DLS value (−1.31). Among these compounds, **3s** demonstrated the most favorable pharmacokinetic properties (Fig. 11).

Based on the previous results, bioavailability radar visualization was used to predict the oral bioavailability of the investigated ligands.

The results showed that all compounds failed the oral bioavailability test. The pink area of the plot defines the drug-likeness of compounds limits for the six physicochemical properties: lipophilicity, size, polarity, solubility, flexibility, and saturation.

Experimental

General information

Chemical methods. All chemicals and solvents were purchased from common commercial sources and were used as received without any further purification. All reactions were monitored by TLC on silica Merck 60 F254 percolated aluminum plates and were developed by spraying with ninhydrin solution (10% in EtOH). Proton nuclear magnetic resonance (^{1}H NMR) spectra were recorded on a Brücker spectrometer at 400 MHz. Chemical shifts are reported in δ units (ppm) with TMS as reference (δ 0.00). All coupling constants (J) are reported in Hertz. Multiplicity is indicated by one or more of the following: s (singlet), d (doublet), dd (doublet

Table 8 Pharmacokinetic parameters and drug likeness score (DLS) of compounds (**3a–3t**) and rhodomyrtone drug[a]

Properties	Molecular weight (g mol^{-1})	Rotatable bonds	H-bond donor	H-bond acceptor	Violations	log Po/W i log P	log S ESOL	GI	BBB	log K_p	Bioavailability score	TPSA (Å)	DLS
Rhodomyrtone	442.54	5	2	6	0	3.76	−6.02	High	No	−4.91	0.56	100.90	−0.33
3a	350.45	1	0	3	0	3.40	−4.62	High	Yes	−5.62	0.85	43.37	−1.31
3b	429.35	1	0	3	0	3.81	−5.54	High	Yes	−5.54	0.85	43.37	−1.17
3d	368.44	1	0	4	0	3.54	−4.79	High	Yes	−5.66	0.85	43.37	−0.98
3c	384.90	1	0	3	0	3.71	−5.22	High	Yes	−5.38	0.85	43.37	−0.77
3e	366.45	1	1	4	0	3.16	−4.48	High	Yes	−5.97	0.85	63.60	−0.72
3f	400.51	1	0	3	0	3.61	−5.79	High	No	−5.04	0.85	43.37	−1.10
3g	410.50	3	0	5	0	3.85	−4.80	High	Yes	−6.93	0.85	61.83	−0.41
3h	364.48	1	0	3	0	3.44	−4.93	High	Yes	−5.45	0.85	43.37	−0.99
3i	384.90	1	0	3	0	3.62	−5.22	High	Yes	−4.13	0.85	43.37	−0.87
3j	366.45	1	1	4	0	3.02	−4.48	High	Yes	−5.97	0.85	63.60	−0.78
3k	395.45	2	0	5	0	3.07	−4.71	High	No	−6.01	0.56	89.19	−1.25
3l	310.34	1	1	4	0	2.40	−3.12	High	Yes	−6.81	0.85	63.60	−0.54
3m	373.24	1	0	3	0	3.09	−4.17	High	Yes	−6.45	0.85	43.37	−0.99
3n	312.33	1	0	4	0	2.83	−3.42	High	Yes	−6.49	0.85	43.37	−0.80
3o	328.79	1	0	3	0	3.00	−3.85	High	Yes	−6.23	0.85	43.37	−0.62
3p	294.34	1	0	3	0	2.70	−3.26	High	Yes	−6.46	0.85	43.37	−1.16
3q	362.34	2	0	6	0	3.06	−5.38	High	No	−6.25	0.85	43.37	−1.04
3r	308.37	1	0	3	0	2.88	−3.56	High	Yes	−6.29	0.85	43.37	−0.63
3s	354.40	3	0	5	0	3.15	−3.43	High	Yes	−6.86	0.85	61.83	0.07
3t	339.34	2	0	5	0	2.70	−3.33	High	No	−6.86	0.56	89.19	−0.98

[a] log Po/W i log P: the octanol/water partition coefficient, log S ESOL: the decimal logarithm of the molar solubility in water, BBB: blood–brain barrier, log K_p: the skin permeability coefficient, TPSA (Å): the topological polar surface area, DLS: dynamic lipophilicity.

of doublets), t (triplet), td (triplet of doublets), q (quartet), m (multiplet). Carbon nuclear magnetic resonance (^{13}C NMR) spectra were recorded on a Brücker at 100 MHz. Chemical shifts are reported in δ units (ppm) relative to DMSO-d$_6$ (δ 39.52). Infrared spectra were recorded on a PerkinElmer 600 spectrometer. Melting points were recorded on a Büchi B-545 apparatus in open capillary tubes. Ultrasound assisted reactions were carried out using a FUNGILAB ultrasonic bath with a frequency of 40 kHz and a nominal power of 250 W. New paragraph: use this style when you need to begin a new paragraph.

General procedure for the preparation of xanthene derivatives. In an open glass tube with a diameter of 25 mm, a thickness of 1 mm, and a volume of 20 mL, a mixture comprising various aromatic aldehydes (1 mmol) and dimedone (2 mmol) or 1,3-cyclohexanedione (2 mmol) was subjected to ultrasound irradiation for an appropriate duration (as detailed in Table 4). This reaction was conducted in the presence of 10% mol of Zn(OAc)$_2$, serving as the catalyst, and ethanol as the solvent. The progress of the reaction was monitored using thin-layer chromatography (TLC) on silica gel plates with a dichloromethane : acetone (9 : 1) eluent.

Upon completion of the reaction, when the TLC indicated the desired outcome, Zn(OAc)$_2$ was precipitated and then filtered out. Subsequently, the reaction mixture was concentrated by evaporation under vacuum. To isolate the pure product, a mixture of diethyl ether and n-hexane in a 6 : 4 ratio was added to the concentrated solution. The solution was then subjected to overnight cooling at 6 °C, leading to the crystallization of the desired product. This procedure was conducted to synthesize and isolate all compounds.

3,3,6,6-Tetramethyl-9-phenyl-3,4,5,6,7,9-hexahydro-1H-xanthene-1,8(2H)-dione (3a). The product (**3a**, C$_{23}$H$_{26}$O$_3$) was obtained as a white powder; 95% yield; R_f = 0.71 (DCM/acetone) (9 : 1); FT-IR (KBr, cm^{-1}): 1667 (C=O), 1458 (C=C); ^{1}H NMR (400 MHz, CDCl$_3$) δ 0.99 (s, 6H, 2CH$_3$), 1.10 (s, 6H, 2CH$_3$), 2.12–2.20 (q, J_{H-H} = 16.4 Hz, 4H, 2CH$_2$-C=C), 2.46 (s, 4H, 2CH-CO), 4.75 (s, 1H, *CH), 7.09 (t, J_{H-H} = 7.6 Hz, 1H, CH$_{Ar}$), 7.20 (t, J_{H-H} = 6.4 Hz, 2H, 2CH$_{Ar}$), 7.28 (t, J_{H-H} = 6.4 Hz, 2H, 2CH$_{Ar}$) ppm; ^{13}C NMR (100 MHz, CDCl$_3$) δ 27.5 (2CH$_3$), 29.4 (2CH$_3$), 31.9 (2C-(CH$_3$)$_2$), 32.3 (2CH$_2$-C=C), 41.0 (*CH), 50.9 (2CH$_2$-CO), 115.8 (2C=CO), 126.4 (CH$_{Ar}$), 128.1 (CH$_{Ar}$), 128.5 (CH$_{Ar}$), 144.2 (C$_{Ar}$), 162.3 (2C-O), 196.4 (2CO) ppm.

9-(4-Bromophenyl)-3,3,6,6-tetramethyl-3,4,5,6,7,9-hexahydro-1H-xanthene-1,8(2H)-dione (3b). The product (**3b**, C$_{23}$H$_{23}$O$_3$Br) was obtained as a white cristal; 93% yield; R_f = 0.78 (DCM/acetone) (9 : 1); FT-IR (KBr, cm^{-1}): 1662 (C=O), 1469 (C=C); ^{1}H NMR (400 MHz, CDCl$_3$) δ 0,98 (s, 6H, 2CH$_3$), 1.03 (s, 6H, 2CH$_3$), 2.08 (d, J_{H-H} = 8.0 Hz, 2H, CH$_2$-C=C), 2.25 (d, J_{H-H} = 8.0 Hz, 2H, CH$_2$-C=C), 2.50–2.56 (m, 4H, 2CH$_2$-CO), 4.50 (s, 1H, *CH), 7.20 (d, J_{H-H} = 7.8 Hz, 2H, 2CH$_{Ar}$), 7.28 (d, J_{H-H} = 7.8, 2H, 2CH$_{Ar}$) ppm; ^{13}C NMR (100 MHz, CDCl$_3$) δ 26.9 (2CH$_3$), 29.0 (2CH$_3$), 31.4 (2C-(CH$_3$)$_2$), 32.3 (2CH$_2$-C=C), 40.6 (*CH), 50.4 (2CH$_2$-CO), 114.4 (2C-CO), 128.3 (CH$_{Ar}$), 130.3 (CH$_{Ar}$), 134.7 (C$_{Ar}$-Br), 143.7 (C$_{Ar}$), 163.5 (2C-O), 196.5 (2CO) ppm.

9-(4-Chlorophenyl)-3,3,6,6-tetramethyl-3,4,5,6,7,9-hexahydro-1H-xanthene-1,8(2H)-dione (3c). The product (**3c**, C$_{23}$H$_{23}$O$_3$Cl) was obtained as a white powder; 94% yield; R_f = 0.80 (DCM/acetone) (9 : 1); FT-IR (KBr, cm^{-1}): 1665 (C=O), 1467 (C=C); ^{1}H NMR (400 MHz, CDCl$_3$) δ 0,99 (s, 6H, 2CH$_3$), 1.09 (s, 6H, 2CH$_3$), 2.12–2.25 (q, 4H, J_{H-H} = 16.4 Hz, 2CH$_2$-C=C), 2.45 (s, 4H, 2CH$_2$-C=O), 4.66 (s, 1H, *CH), 6.53 (d, J_{H-H} = 8.4 Hz, 2H,

Fig. 11 Radar related to physicochemical properties of the synthesized molecules, rhodomyrtone drug and DLS score.

2CH$_{Ar}$), 7.05 (d, J_{H-H} = 8.0 Hz, 2H, 2CH$_{Ar}$) ppm; ^{13}C NMR (100 MHz, CDCl$_3$) δ 27.5 (2CH$_3$), 28.5 (2CH$_3$), 30.6 (2C-(CH)$_2$), 32.3 (2CH$_2$-C=C), 41.0 (*CH), 49.2 (2CH$_2$-CO), 115.3 (2C-CO), 117.1

(2CH$_{Ar}$), 129.4 (2CH$_{Ar}$), 135.3 (C$_{Ar}$-Cl), 155.2 (C$_{Ar}$), 163.4 (C-O), 195.7 (2CO) ppm.

9-(4-Fluorophenyl)-3,3,6,6-tetramethyl-3,4,5,6,7,9-hexahydro-1H-xanthene-1,8(2H)-dione (3d). The product (3d, C$_{23}$H$_{23}$O$_3$F) was obtained as a white powder; 92% yield; R_f = 0.81 (DCM/acetone) (9 : 1); FT-IR (KBr, cm^{-1}): 1659 (C=O), 1507 (C=C); ^{1}H NMR (400 MHz, CDCl$_3$) δ 0,94 (s, 6H, 2CH$_3$), 1.08 (s, 6H, 2CH$_3$), 2.00 (d, J_{H-H} = 7.8 Hz, 2H, CH$_2$-C=C), 2.26 (d, J_{H-H} = 8.0 Hz, 2H, CH$_2$ C=C), 2.52–2.57 (m, 4H, 2CH$_2$-CO), 4.51 (s, 1H, *CH), 7.01–7.15 (m, 2H, 2CH$_{Ar}$), 7.20–7.25 (m, 2H, 2CH$_{Ar}$) ppm; ^{13}C NMR (100 MHz, CDCl$_3$) δ 26.9 (2CH$_3$), 29.1 (2CH$_3$), 31.1 (2C-(CH$_3$)$_2$), 32.2 (2CH$_2$-C=C), 40.4 (*CH), 50.5 (2CH$_2$-CO), 114.6 (2C-CO), 114.9 (CH$_{Ar}$), 115.2 (CH$_{Ar}$), 130.3 (d, J_{C-F} = 9.0 Hz, C$_{Ar}$-F), 140.9 (C$_{Ar}$), 163.4 (2C-O), 196.5 (2CO) ppm.

9-(4-Hydroxyphenyl)-3,3,6,6-tetramethyl-3,4,5,6,7,9-hexahydro-1H-xanthene-1,8(2H)-dione (3e). The product (3e, C$_{23}$H$_{26}$O$_4$) was obtained as a white powder; 88% yield; R_f = 0.80 (DCM/acetone) (9 : 1); FT-IR (KBr, cm^{-1}): (OH) 3411, 1659 (C=O), 1512 (C=C); ^{1}H NMR (400 MHz, CDCl$_3$) δ 1,00 (s, 6H, 2CH$_3$), 1.09 (s, 6H, 2CH$_3$), 2.16–2.27 (q, 4H, J_{H-H} = 16.4 Hz, 2CH$_2$-C=C), 2.45 (s, 4H, 2CH$_2$-CO), 4.67 (s, 1H, *CH), 6.29 (s, 1H, OH), 6.55 (d, J_{H-H} = 8.8 Hz, 2H, 2CH-Ar), 7.06 (d, J_{H-H} = 8.8 Hz, 2H, 2CH-Ar) ppm; ^{13}C NMR (100 MHz, CDCl$_3$) δ 26.8 (2CH$_3$), 29.3 (2CH$_3$), 31.9 (2C-(CH$_3$)$_2$), 33.0 (2CH$_2$-C=C), 41.0 (*CH), 50.9 (2CH$_2$-CO), 115.3 (2C-CO), 116.5 (CH$_{Ar}$), 130.3 (CH$_{Ar}$), 136.4 (C$_{Ar}$), 154.7 (C$_{Ar}$-OH), 162.9 (2C-O), 197.5 (2CO) ppm.

3,3,6,6-Tetramethyl-9-(naphthalen-1-yl)-3,4,5,6,7,9-hexahydro-1H-xanthene-1,8(2H)-dione (3f). The product (3f, C$_{27}$H$_{28}$O$_3$) was obtained as a white powder; 89% yield; R_f = 0.70 (DCM/acetone) (9 : 1); FT-IR (KBr, cm^{-1}): 1668 (C=O), 1508 (C=C); ^{1}H NMR (400 MHz, CDCl$_3$) δ 0.99 (s, 6H, 2CH$_3$), 1.11 (s, 6H, 2CH$_3$), 2.12–2.26 (q, 4H, J_{H-H} = 16.4 Hz, 2CH$_2$-C=C), 2.50 (s, 4H, 2CH$_2$-CO), 4.92 (s, 1H, *CH), 7.34–7.46 (m, 3H, 3CH$_{Ar}$), 7.69–7.77 (m, 4H, 4CH$_{Ar}$) ppm; ^{13}C NMR (100 MHz, CDCl$_3$) δ 27.4 (2CH$_3$), 29.4 (2CH$_3$), 32.1 (2C-(CH$_3$)$_2$), 32.3 (CH-C=C), 41.1 (*CH), 50.9 (2CH$_2$-CO), 115.8 (2C-CO), 125.4 (CH$_{Ar}$), 125.7 (CH$_{Ar}$), 127.0 (CH$_{Ar}$), 127.2 (CH$_{Ar}$), 127.6 (CH$_{Ar}$), 127.8 (CH$_{Ar}$), 128.1 (CH$_{Ar}$), 132.5 (C$_{Ar}$), 133.5 (C$_{Ar}$), 141.7 (C$_{Ar}$), 162.4 (2C-O), 196.4 (2CO) ppm.

9-(3,4-Dimethoxyphenyl)-3,3,6,6-tetramethyl-3,4,5,6,7,9-hexahydro-1H-xanthene-1,8(2H)-dione (3g). The product (3g, C$_{25}$H$_{30}$O5) was obtained as a white powder; 86% yield; R_f = 0.80 (DCM/acetone) (9 : 1); FT-IR (KBr, cm^{-1}): 1644 (C=O), 1514 (C=C); ^{1}H NMR (400 MHz, DMSO-d$_6$) δ, 0.97 (s, 6H, 2CH$_3$), 1.09 (s, 6H, 2CH$_3$), 2.11 (d, J_{H-H} = 16.0 Hz, 2H, CH$_2$–C=C), 2.26 (d, J_{H-H} = 16.2 Hz, 2H, CH$_2$-C=C), 2.55 (q, J_{H-H} = 17.6 Hz, 4H, 2CH$_2$-CO), 3.72 (s, 6H, 2CH$_3$-O), 4.52 (s, 1H, *CH), 6.94–6.56 (m, 3H, 3CH$_{Ar}$) ppm; ^{13}C NMR (100 MHz, DMSO-d$_6$) δ 26.4 (2CH$_3$), 28.6 (2CH$_3$), 30.4 (2C-(CH$_3$)$_2$), 31.6 (2CH$_2$-C=C), 39.8 (*CH), 49.5 (2CH$_2$-CO), 55.3 (2CH$_3$-O), 111.2 (CH$_{Ar}$), 111.8 (CH$_{Ar}$), 114.5 (2C-CO), 118.4 (CH$_{Ar}$), 136.7 (C$_{Ar}$), 147.1 (C$_{Ar}$-OCH$_3$), 148.0 (C$_{Ar}$-OCH$_3$), 162.7 (2C-O), 196.7 (2CO) ppm.

3,3,6,6-Tetramethyl-9-(m-tolyl)-3,4,5,6,7,9-hexahydro-1H-xanthene-1,8(2H)-dione (3h). The product (3h, C$_{24}$H$_{28}$O$_3$) was obtained as a white powder; 89% yield; R_f = 0.75 (DCM/acetone) (9 : 1); FT-IR (KBr, cm^{-1}): 1667 (C=O), 1463 (C=C); ^{1}H NMR (400 MHz, CDCl$_3$) δ 0.99 (s, 6H, 2CH$_3$), 1.10 (s, 6H, 2CH$_3$), 2.14–

2.24 (q, 4H, J_{H-H} = 16.2 Hz (CH$_2$-C=C), 2.28 (s, 3H, CH$_3$), 2.46 (s, 4H, 2CH$_2$-CO), 4.71 (s, 1H, *CH), 6.89 (d, J_{H-H} = 7.2 Hz, 1H, CH$_{Ar}$), 7.01 (d, J_{H-H} = 8.0 Hz, 1H, CH$_{Ar}$), 7.06–7.13 (m, 2H, 2CH$_{Ar}$) ppm; ^{13}C NMR (100 MHz, CDCl$_3$) δ 21.6 (CH$_3$-Ar), 27.5 (2CH$_3$), 29.4 (2CH$_3$), 31.9 (2C-(CH$_3$)$_2$), 32.4 (2CH$_2$-C=C), 41.1 (*CH), 51.0 (2CH$_2$-CO), 116.0 (2C-CO), 125.4 (CH$_{Ar}$), 127.5 (CH$_{Ar}$), 128.1 (CH$_{Ar}$), 129.6 (CH$_{Ar}$), 137.6 (C$_{Ar}$-CH$_3$), 144.2 (C$_{Ar}$), 162.4 (2C-O), 197.0 (2CO) ppm.

9-(2-Chlorophenyl)-3,3,6,6-tetramethyl-3,4,5,6,7,9-hexahydro-1H-xanthene-1,8(2H)-dione (3i). The product (3i, C$_{23}$H$_{23}$O$_3$Cl) was obtained as a white powder; 87% yield; R_f (DCM/acetone) (9 : 1); FT-IR (KBr, cm^{-1}): 1665 (C=O), 1467 (C=C) ^{1}H NMR (400 MHz, CDCl$_3$) δ 1,01 (s, 6H, 2CH$_3$), 1.09 (s, 6H, 2CH$_3$), 2.13–2.24 (q, 4H, J_{H-H} = 16.4 Hz, 2CH$_2$-C=C), 2.42 (s, 4H, 2CH$_2$-C=O), 4.99 (s, 1H, *CH), 7.05 (t, 1H, J_{H-H} = 7.6 Hz, CH$_{Ar}$), 7.16 (t, 1H, J_{H-H} = 7.6 Hz, CH$_{Ar}$), 7.21 (d, 1H, J_{H-H} = 7.6 Hz, CH$_{Ar}$), 7.42 (d, 1H, J_{H-H} = 7.6 Hz, CH$_{Ar}$) ppm; ^{13}C NMR (100 MHz, CDCl$_3$) δ 27.5 (2CH$_3$), 29.4 (2CH$_3$), 31.8 (2C-(CH$_3$)$_2$), 32.8 (2CH$_2$-C=C), 40.9 (*CH), 50.8 (2CH$_2$-CO), 113.8 (2C-CO), 126.4 (CH$_{Ar}$), 128.5 (CH$_{Ar}$), 129.2 (CH$_{Ar}$), 130.3 (CH$_{Ar}$), 132.5 (C$_{Ar}$-Cl), 140.1 (C$_{Ar}$), 163.0 (2C-O), 196.1 (2CO) ppm.

9-(2-Hydroxyphenyl)-3,3,6,6-tetramethyl-3,4,5,6,7,9-hexahydro-1H-xanthene-1,8(2H)-dione (3j). The product (3j, C$_{23}$H$_{26}$O$_4$) was obtained as a white powder; 84% yield; R_f = 0.8 (DCM/acetone) (9 : 1); FT-IR (KBr, cm^{-1}): 3400 (OH), 1637 (C=O), 1458 (C=C); ^{1}H NMR (400 MHz, CDCl$_3$) δ 0,99 (s, 6H, 2CH$_3$), 1.03 (s, 3H, CH$_3$), 1.12 (s, 3H, CH$_3$), 1.90–2.00 (q, 2H, J_{H-H} = 16.4 Hz, CH$_2$-C=C), 2.33 (s, 2H, CH$_2$-C=C), 2.35–2.61 (q, 4H, J_{H-H} = 17.6 Hz, 2CH$_2$-C=O), 4.76 (s, 1H, *CH), 6.95–7.07 (m, 3H, CH$_{Ar}$), 7.11–7.19 (m, 1H, H$_{Ar}$), 10.44 (s, 1H, OH) ppm; ^{13}C NMR (100 MHz, CDCl$_3$) δ 27.3 (CH$_3$), 27.9 (CH$_3$), 29.2 (CH$_3$), 29.9 (CH$_3$), 31.1 (2C-(CH$_3$)$_2$), 32.4 (2CH$_2$-C=C), 41.7 (2CH$_2$ C=C), 50.0 (*CH), 50.8 (2CH$_2$-CO), 111.2 (2C-CO), 115.9 (CH$_{Ar}$), 124.7 (CH$_{Ar}$), 127.6 (CH$_{Ar}$), 128.1 (CH$_{Ar}$), 151.2 (C$_{Ar}$), 169.2 (2C-O), 170.7 (C-OH), 201.0 (CO) ppm.

9-(4-Fluorophenyl)-3,4,5,6,7,9-hexahydro-1H-xanthene-1,8(2H)-dione (3n). The product (3n, C$_{19}$H$_{17}$FO$_3$) was obtained as a white powder; 92% yield; R_f = 0.75 DCM/acetone) (9 : 1); FT-IR (KBr, cm^{-1}): 1656 (C=O), 1501 (C=C); ^{1}H NMR (400 MHz, DMSO-d$_6$) δ 1.82–1.89 (m, 2H, CH$_2$-CH$_2$), 1.91–2.00 (m, 2H, CH$_2$-CH$_2$), 2.25–2.33 (m, 4H, 2CH$_2$-C=C), 2.53–2.69 (m, 4H, 2CH$_2$-C=C), 4.57 (d, J_{H-F} = 11.9 Hz, 1H, *CH), 6.94 (t, J_{H-H} = 8.6 Hz, 1H, CH$_{Ar}$), 7.15 (d, J_{H-H} = 8.0 Hz, 1H, CH$_{Ar}$), 7.24 (t, J_{H-H} = 6.0 Hz, 1H, CH$_{Ar}$), 7.33 (d, J_{H-H} = 8.0 Hz, 1H, CH$_{Ar}$) ppm; ^{13}C NMR (100 MHz, DMSO-d$_6$) δ 20.7 (2CH$_2$-CH$_2$), 26.9 (2CH$_2$-C=C), 34.2 (2CH$_2$-CO), 50.7 (*CH), 112.9 (2C-CO), 114.1 (CH$_{Ar}$), 115.0 (CH$_{Ar}$), 116.0 (CH$_{Ar}$), 129.5 (CH$_{Ar}$), 130.5 (C$_{Ar}$), 163.9 (2C-O), 164.5 (C-F), 195.8 (CO), 205.6 (CO) ppm.

9-(4-Chlorophenyl)-3,4,5,6,7,9-hexahydro-1H-xanthene-1,8(2H)-dione (3o). The product (3o, C$_{19}$H$_{17}$ClO$_3$) was obtained as a yellow powder; 93% yield; R_f = 0.74 (DCM/acetone) (9 : 1); FT-IR (KBr, cm^{-1}): 1645 (C=O),1510 (C=C); ^{1}H NMR (400 MHz, DMSO-d$_6$) δ 1.83–1.96 (m, 4H, 2CH$_2$-CH$_2$), 2.23–2.30 (m, 4H, 2CH$_2$-C=C), 2.60–2.68 (m, 4H, 2CH$_2$-CO), 4.50 (s, 1H, *CH), 6.58 (d, J_{H-H} = 8.0 Hz, 2H, 2CH$_{Ar}$), 6.97 (d, J_{H-H} = 8.0 Hz, 2H, 2CH$_{Ar}$) ppm; ^{13}C NMR (100 MHz, DMSO-d$_6$) δ 20.6 (2CH$_2$-CH$_2$), 26.3 (2CH$_2$-C=C), 30.9 (2CH$_2$-CO), 35.3 (*CH), 113.9 (2C-CO),

117.1 (CH$_{Ar}$), 128.7 (CH$_{Ar}$), 135.7 (C-Cl), 157.1 (C$_{Ar}$), 163.9 (2C-O), 196.2 (2CO) ppm.

9-(4-Hydroxyphenyl)-3,4,5,6,7,9-hexahydro-1H-xanthene-1,8(2H)-dione (3p). The product (3p, C$_{19}$H$_{18}$O$_4$) was obtained as a white powder; 89% yield; R_f = 0.85 (DCM/acetone) (9 : 1); FT-IR (KBr, cm^{-1}): 3353 (OH), 1644 (C=O), 1512 (C=C),^{1}H NMR (400 MHz, DMSO-d$_6$) δ 1.79–1.98 (m, 4H, 2CH$_2$-CH$_2$), 2.21–2.30 (m, 4H, 2CH$_2$-C=C), 2.54–2.69 (m, 4H, 2CH$_2$-CO), 4.49 (s, 1H, *CH), 6.57 (d, J_{H-H} = 8.0 Hz, 2H, 2CH$_{Ar}$), 6.95 (d, J_{H-H} = 8.0 Hz, 2H, 2CH$_{Ar}$), 9.09 (s, 1H, OH) ppm; ^{13}C NMR (101 MHz, DMSO-d$_6$) δ 19.8 (2CH$_2$-CH$_2$), 26.3 (2CH$_2$-C=C), 29.7 (2CH$_2$-CO), 36.0 (*CH), 114.6 (2C-CO), 116.9 (CH$_{Ar}$), 128.7 (CH$_{Ar}$), 135.6 (C-Cl), 155.9 (C$_{Ar}$), 163.6 (2C-O), 195.8 (2CO) ppm.

9-(4-(Trifluoromethyl)phenyl)-3,4,5,6,7,9-hexahydro-1H-xanthene-1,8(2H)-dione (3q). The product (3q, C$_{24}$H$_{25}$F$_3$O$_3$) was obtained as a white powder; 90% yield; R_f = 0.73 (DCM/acetone) (9 : 1); FT-IR (KBr, cm^{-1}): 1663 (C=O), 1420 (C=C); ^{1}H NMR (400 MHz, CDCl$_3$) δ 1.96–2.11 (m, 4H, 2CH$_2$-CH$_2$), 2.27–2.42 (m, 4H, 2CH$_2$-C=C), 2.54–2.74 (m, 4H, 2CH$_2$-CO), 4.85 (s, 1H, *CH), 7.41 (d, J_{H-H} = 8.2 Hz, 2H, 2CH$_{Ar}$), 7.47 (d, J_{H-H} = 8.2 Hz, 2H, 2CH$_{Ar}$) ppm; ^{13}C NMR (100 MHz, CDCl$_3$) δ 20.4 (2CH$_2$-CH$_2$), 27.2 (2CH$_2$-C=C), 33.0 (2CH$_2$-CO), 37.0 (*CH), 116.4 (2C-CO), 125.2 (CF$_3$), 130.1 (C-CF$_3$), 128.9 (CH$_{Ar}$), 149.3 (C$_{Ar}$), 164.4 (2C-O), 196.5 (2CO) ppm.

9-(m-Tolyl)-3,4,5,6,7,9-hexahydro-1H-xanthene-1,8(2H)-dione (3r). The product (3r, C$_{20}$H$_{20}$O$_3$) was obtained as a white powder; 87% yield; R_f = 0.77 (DCM/acetone) (9 : 1); FT-IR (KBr, cm^{-1}): 1665 (C=O), 1486 (C=C), ^{1}H NMR (400 MHz, CDCl$_3$) δ 1.94–2.05 (m, 4H, 2CH$_2$-CH$_2$), 2.25–2.38 (m, 4H, 2CH$_2$-C=C), 2.28 (s, 3H, CH$_3$), 2.50–2.66 (m, 4H, 2CH$_2$-CO), 4.77 (s, 1H, *CH), 6.91 (d, J_{H-H} = 7.6 Hz, 1H, CH$_{Ar}$), 7.02 (d, J_{H-H} = 8.0 Hz, 1H, CH$_{Ar}$), 7.07 (d, J_{H-H} = 7.6 Hz, 1H, CH$_{Ar}$), 7.12 (s, 1H, CH$_{Ar}$) ppm; ^{13}C NMR (100 MHz, CDCl$_3$) δ 20.4 (2CH$_2$-CH$_2$), 21.5 (CH$_3$), 27.2 (2CH$_2$-C=C), 31.6 (2CH$_2$-CO), 37.0 (*CH), 117.1 (2C-CO), 125.3 (CH$_{Ar}$), 127.9 (CH$_{Ar}$), 128.0 (CH$_{Ar}$), 129.4 (CH$_{Ar}$), 137.5 (C-CH$_3$), 143.6 (C$_{Ar}$), 163.9 (2C-O), 196.5 (2CO) ppm.

9-(3,4-Dimethoxyphenyl)-3,4,5,6,7,9-hexahydro-1H-xanthene-1,8(2H)-dione (3s). The product (3s, C$_{21}$H$_{22}$O$_5$) was obtained as a white powder; 85% yield; R_f = 0.82 (DCM/acetone) (9 : 1); FT-IR (KBr, cm^{-1}): 1668 (C=O), 1512 (C=C); ^{1}H NMR (400 MHz, DMSO-d$_6$) δ 1.81–1.99 (m, 4H, 2CH$_2$-CH$_2$), 2.24–2.39 (m, 4H, 2CH$_2$-C=C), 2.54–2.69 (m, 4H, 2CH$_2$-CO), 3.67 (s, 3H, O-CH$_3$), 3.69 (s, 3H, O-CH$_3$), 4.54 (s, 1H, *CH), 6.63 (d, J_{H-H} = 6.0 Hz, 1H, CH$_{Ar}$), 6.76 (J_{H-H} = 7.6 Hz, 2H, 2CH$_{Ar}$) ppm; ^{13}C NMR (100 MHz, DMSO-d$_6$) δ 19.8 (2CH$_2$-CH$_2$), 26.3 (2CH$_2$-C=C), 29.6 (2CH$_2$-CO), 37.6 (*CH), 56.7 (2CH$_3$-O), 111.6 (CH$_{Ar}$), 113.3 (CH$_{Ar}$), 115.9 (CH$_{Ar}$), 119.6 (2C-CO), 137.1 (C$_{Ar}$), 146.9 (C-OCH$_3$), 148.1 (C-OCH$_3$), 165.9 (2C-O), 197.1 (2CO) ppm.

X-ray crystallography

Crystallographic data for the studied compound 3r was collected on a SuperNova, Dual, Cu at home/near, AtlasS2 four-circle diffractometer equipped with an AtlasS2 CCD detector using Cu Kα (micro-focus sealed tube) radiation (λ = 1.54184 Å), the crystal was kept at a temperature of 295 K during data collection.

The crystallographic data and experimental details for structural analysis are summarized in Table 9. The reported structure was solved with the SHELXT-2014/5 (ref. 47) solution program by Intrinsic Phasing with Olex2 (ref. 48) as the graphical interface. The model was refined with SHELXL-2018/3 (ref. 49) using full matrix least-squares minimization on F2. All absorption corrections were performed with the CrysAlisPro 1.171.42.51a[50] using spherical harmonics implemented in SCALE3 ABSPACK scaling algorithm. Crystal structure visualization and construction of crystal packing diagrams were performed using Mercury 4.0 software.[51]

CCDC number: 2308384 contains the supplementary crystallographic data for compound **3r**.[52]

Computational methods

Molecular docking. The X-ray crystal structure of the VEGFR-2 enzyme and the 4-amino-furo[2,3-*d*] pyrimidine complex (PDB ID 1YWN) was obtained from the RSC Protein Data Bank.[53] The structure was prepared using the Protein Preparation Wizard in the Schrödinger Suites software package. The three-dimensional structures of the derivatives were generated using Maestro software and further optimized with Ligprep using the OPLS3e force field.[54] The final prepared PDB files for both the protein and the synthesized compounds were submitted for the docking process. Docking studies were conducted using the Glide software with standard precision settings.[55] The output files containing the docked compounds

Table 9 Crystallographic data and refinement parameters of compound **3r**

Moiety formula	$C_{20}H_{20}O_3$
Sum formula	$C_{20}H_{20}O_3$
Formula weight (g mol^{-1})	308.36
Crystal habit, color	Needle, colourless
Crystal system	Orthorhombic
Space group	$Pca2_1$
a (Å)	18.2645(5)
b (Å)	9.2078(2)
c (Å)	9.6666(2)
α (°)	90
β (°)	90
γ (°)	90
Volume (Å^3)	1625.69(7)
Z, Z'	4, 0
Density (calculated) (g cm^{-3})	1.260
Absorption coefficient (mm^{-1})	0.670
$F(000)$	656.0
Crystal size (mm)	$0.22 \times 0.04 \times 0.02$
2θ range for data collection (°)	9.606 to 149.024
Reflections collected	6225
Independent reflections	2390
R_{int}	0.0363
Number of parameters	209
Goodness-of-fit on F^2	1.045
Final R indices $[I \geq 2\sigma(I)]$	$R_1 = 0.042$, w$R_2 = 0.1010$
R indexes [all data]	$R_1 = 0.0555$, w$R_2 = 0.1106$
Largest difference peak and hole (Å^3)	0.13, −0.12
CCDC deposition no.	CCDC 2308384

in complex with the VEGFR-2 enzyme were visualized using Chimera X.[56]

Molecular dynamics simulation. Molecular Dynamics (MD) simulations were performed using Desmond on Schrödinger academic software-2022 and OPLS-2005 (ref. 57) and the simulations were carried out on a Linux environment, utilizing an Intel Core i5-13400F CPU operating at 4.60 GHz and an Nvidia GeForce RTX 3060 12 GB GPU.

The docking complexes for the **3e** and **3p** compounds were taken as the initial coordinates for MD simulations. A 10 Å orthorhombic box with a dimension of $10.0 \times 10.0 \times 10.0$ nm^3 employed TIP3P model contains 10 567 water molecules/36 350 atoms for **3e**, and 10 551 water molecules/36 290 **3p** was used for the solvation of the system with OPLS-2005 force field. To neutralize the system, sodium ions were introduced as counter ions. Following solvation, the system underwent energy minimization, with a convergence threshold set at 1 kcal mol^{-1} Å^{-1}. Subsequently, pre-equilibration was performed using Desmond's default six-step relaxation protocol. The initial two steps involved energy minimization, with the first step restraining the solute and the second step removing these restraints. The subsequent steps consisted of short MD simulations, each lasting 12 ps, 12 ps, and 24 ps, respectively, within the NPT ensemble at temperatures of 10 K, 10 K, 300 K, and 300 K.

A 200 ns MD simulation production run was then executed, applying periodic boundary conditions and simulating under isothermal and isobaric conditions with a relaxation time of 0.2 ps. The MD simulation was pivotal in identifying regions of the protein influenced by the presence of the ligand, making it valuable for validating docking poses. The simulations treated the entire protein–ligand system as flexible, providing insights into potential conformational changes and binding interactions.

Visualization of the protein–ligand complexes and analysis of the MD trajectory were carried out using Maestro. In-depth analyses were conducted using Desmond's Simulation Event Analysis tool, offering a comprehensive exploration of the simulation data.[58]

DFT study. The gas phase structure optimization of xanthene derivatives (**3a–3t**) is optimized using DFT at B3LYP method,[59] with the basis set of 6-31G(d,p) implemented by Gaussian 09 package.[60] Frontier molecular orbitals and global reactivity descriptors the highest occupied molecular orbital (HOMO) and lowest un-occupied molecular orbital (LUMO),[61] energy gap and chemical reactivity descriptors are calculated at DFT/B3LYP/6-31G(d,p) method.

Pharmacokinetics analysis ADME. One significant contribution in this field was made by Lipinski *et al.*,[62] who studied orally active compounds to establish physicochemical ranges that increase the probability of a compound being an oral drug. This approach, known as the Rule-of-Five, established a correlation between pharmacokinetic and physicochemical parameters.

Regarding this part of the work, we used the SwissADME web tool *via* the link: **https://www.swissadme.ch/**,[63] that offers free access to a pool of quick yet reliable predictive models for physicochemical properties, pharmacokinetics, drug-likeness

and medicinal chemistry friendliness, including in-house effective techniques like the BOILED-Egg, iLOGP, and bioavailability radar. The Drug Likeness Score (DLS) results were determined using the Molsoft web tool *via* the link: **https://www.molsoft.com**.[64]

Conclusion

In summary, we have developed an environmentally friendly and efficient method for synthesizing xanthene derivatives using ultrasound irradiation as an energy source and zinc acetate as a mild catalyst. The synthesized compounds were prepared in high yields (84–95%) within a short reaction time. Structural confirmation of all compounds in this series was established through conventional spectroscopic methods. Additionally, we conducted *in silico* studies on these compounds to determine their significance. The results from the molecular docking study demonstrated satisfactory interactions of the synthesized compounds with the VEGRF-2 enzyme. Furthermore, a molecular dynamics simulation was carried out to validate the binding mode predicted by the molecular docking of compounds **3e** and **3p** within the active site of VEGRF-2. Notably, the two selected ligands exhibited consistent and favorable results, maintaining the same hydrogen bonds and preserving hydrophobic interactions with the residues even after a 200 ns simulation. The compounds were optimized using the DFT-B3LYP method at the 6-31G(d,p) level, revealing interesting energy gaps for most of them, suggesting their potential stability. Furthermore, all compounds were assessed based on the Lipinski Rule of Five for their bioactivity, molecular descriptors, and drug-likeness, demonstrating favorable oral bioavailability.

Data availability

All data generated or analyzed during this study are included in this published article and its ESI files.†

Author contributions

All authors contributed significantly to the design, execution, and interpretation of the reported experiments. Rayene Sayad: wrote the original draft, executed the experimental section, and conducted the ADME study. Abdeslem Bouzina: conducted docking and dynamic studies, played a pivotal role in validation, and contributed to the review and editing process. Yousra Ouafa Bouone: drafted the sections related to Density Functional Theory (DFT) and X-ray analysis. Dounia Beldjezzia: managed the curation of data and conducted formal analysis. Abdelhak Djemel and Malika Ibrahim-Ouali: provided essential resources for the study and conducted analyses of the obtained products (NMR, IR, and X-ray diffraction). Nour-Eddine Aouf and Zineb Aouf: contributed to the review and editing process, covering aspects such as the introduction, results, discussion, and other relevant sections. All authors have read and approved the final manuscript.

Conflicts of interest

There are no conflicts to declare.

Acknowledgements

References

1 (*a*) M. R. Taghartapeh, N. N. Pesyan, H. Rashidnejad, H. R. Khavasi and A. Soltani, *J. Mol. Struct.*, 2017, **1149**, 873; (*b*) L. Jeyaseeli, A. D. Gupta, K. A. Kumar, K. Mazumdar, N. K. Dutta and S. G. Dastidar, *Int. J. Antimicrob. Agents*, 2006, **27**, 62; (*c*) T. Yıldız and H. B. Küçük, *RSC Adv.*, 2017, **7**, 6649.

2 A. Chaudhary and J. M. Khurana, *Curr. Org. Synth.*, 2018, **15**, 369.

3 A. G. Ghahsare, Z. S. Nazifi and S. M. R. Nazifi, *Curr. Org. Synth.*, 2019, **16**, 7.

4 A. S. Burange, K. G. Gadam, P. S. Tugaonkar, S. D. Thakur, R. K. Soni, R. R. Khan, M. S. Tai and C. S. Gopinath, *Environ. Chem. Lett.*, 2021, **19**, 3314.

5 G. Shabir, A. Saeed and P. A. Channar, *Mini-Rev. Org. Chem.*, 2018, **15**, 197.

6 M. Maia, D. I. S. P. Resende, F. Duraes, M. M. M. Pinto and E. Sousa, *Eur. J. Med. Chem.*, 2021, **210**, 113085.

7 R. Sangwan, M. Saini, R. Verma, S. Kumar, M. Banerjee and S. Jain, *J. Mol. Struct.*, 2020, **1208**, 127786.

8 N. Mulakayala, P. V. N. S. Murthy, D. Rambabu, M. Aeluri, R. Adepu, G. R. Krishna, C. M. Reddy, K. R. S. Prasad, M. Chaitanya, C. S. Kumar, M. V. B. Rao and M. Pal, *Bioorg. Med. Chem. Lett.*, 2012, **22**, 2191.

9 J. J. Omolo, M. M. Johnson, S. F. Van Vuuren and C. B. de Koning, *Bioorg. Med. Chem. Lett.*, 2011, **21**, 7088.

10 J. M. Jamison, K. Krabill, A. Hatwalkar, E. Jamison and C. C. Tsai, *Cell Biol. Int. Rep.*, 1990, **14**, 1084.

11 J. M. Khurana, D. Magoo, K. Aggarwal, N. Aggarwal, R. Kumar and C. Srivastava, *Eur. J. Med. Chem.*, 2012, **58**, 477.

12 H. N. Hafez, M. I. Hegab, I. S. Ahmed-Farag and A. B. A. El Gazzar, *Bioorg. Med. Chem. Lett.*, 2008, **18**, 4543.

13 G. S. Shankarling and K. J. Jarag, Laser dyes, *Resonance*, 2010, **15**, 818.

14 (*a*) S. H. Guo, T. H. Leng, K. Wang, C. Y. Wang, Y. J. Shen and W. H. Zhu, *Talanta*, 2018, **185**, 364; (*b*) J. Liu, X. Chen, Y. Zhang, G. Gao, X. Zhang and S. Hou, *J. Lumin.*, 2018, **204**, 484; (*c*) H. Qi, H. Takano, Y. Kato, Q. Wu, C. Ogata, B. Zhu, Y. Murata and Y. Nakamura, *Biochim. Biophys. Acta, Gen. Subj.*, 2011, **1810**, 712; (*d*) T. M. Ebaston, A. Rozovsky, A. Zaporozhets, A. Bazylevich, H. Tuchinsky, V. Marks, G. Gellerman and L. D. Patsenker, *ChemMedChem*, 2019, **14**, 1734.

15 K. M. Khan, I. Khan, S. Perveen and M. I. Malik, *J. Fluorine Chem.*, 2014, **1581**, 5.

16 (*a*) H. F. Niya, N. Hazeri, M. Fatahpour and M. T. Maghsoodlou, *Res. Chem. Intermed.*, 2020, **46**, 3666; (*b*) D. Thirumalai and S. Gajalakshmi, *Res. Chem. Intermed.*, 2020, **46**, 2668; (*c*) N. Srinivasan, A. Yurek-George and A. Ganesan, *Mol. Diversity*, 2005, **9**, 291.

17 D. Prasad, A. Preetam and M. Nath, *C. R. Chim.*, 2013, **16**, 1157.

18 (*a*) M. Salami and A. Ezabadi, *Res. Chem. Intermed.*, 2020, **46**, 4626; (*b*) S. E. S. Sorkhi, M. M. Hashemi and A. Ezabadi, *Res. Chem. Intermed.*, 2020, **46**, 2246; (*c*) H. Naeimi and Z. S. Nazifi, *J. Ind. Eng. Chem.*, 2014, **20**, 1050.

19 E. Yoshioka, S. Kohtani and H. Miyabe, *Angew. Chem., Int. Ed.*, 2011, **50**, 6642.

20 G. Sabitha, K. Arundhathi, K. Sudhakar, B. S. Sastry and J. S. Yadav, *Synth. Commun.*, 2008, **38**, 3446.

21 B. S. Kuarm, J. V. Madhav, S. V. Laxmi, B. Rajitha, Y. T. Reddy, P. N. Reddy and P. A. Crooks, *Synth. Commun.*, 2011, **41**, 669.

22 S. Kantevari, R. Bantu and L. Nagarapu, *Arkivoc*, 2006, **16**, 148.

23 H. Naeimi and Z. S. Nazifi, *J. Ind. Eng. Chem.*, 2013, **20**, 1050.

24 K. Gong, H. Wang, S. Wang, Y. Wang and J. Chen, *Catal.*, 2015, **36**, 1255.

25 H. Eshghi, M. Eftekhar, M. Rahimizadeh, M. Hassanpour and M. Bakavoli, *Org. Chem. Res.*, 2016, **2**, 27.

26 B. Das, K. Laxminarayana, M. Krishnaiah and Y. Srinivas, *Synlett*, 2007, **20**, 3112.

27 P. Zhang, Y. D. Yu and Z. H. Zhang, *Synth. Commun.*, 2008, **38**, 4479.

28 A. Ilangovan, S. Malayappasamy, S. Muralidharan and S. Maruthamuthu, *Chem. Cent. J.*, 2011, **5**, 87.

29 (*a*) R. K. Vohra, J. L. Renaud and C. Bruneau, *Collect. Czech. Chem. Commun.*, 2005, **70**, 1952; (*b*) I. Węglarz, M. Szewczyk and J. Mlynarskia, *Adv. Synth. Catal.*, 2020, **8**, 1536.

30 (*a*) J. Y. Liu, G. E Cao, W. Xu, J. Cao and W. L. Wang, *Appl. Organomet. Chem.*, 2010, **24**, 691; (*b*) Q. Yuancheng, Z. Dan and M. Li, *Lett. Org. Chem.*, 2012, **9**, 272.

31 S. J. Modi and V. M. Kulkarni, *Med. Drug Discovery*, 2019, **2**, 100009.

32 I. V. Machado, J. R. N. dos Santos, M. A. P. Januario and A. G. Corrêa, *Ultrason. Sonochem.*, 2021, **78**, 105704.

33 W. Bonrath, *Ultrason. Sonochem.*, 2005, **12**, 106.

34 N. Mulakayala, G. P. Kumar, D. Rambabu, M. Aeluri, M. V. B. Rao and M. Pal, *Tetrahedron Lett.*, 2012, **53**, 6926.

35 S. Rostamizadeh, A. M. Amani, G. H. Mahdavinia, G. Amiri and H. Sepehrian, *Ultrason. Sonochem.*, 2010, **17**, 309.

36 S. Kumari, A. Shekhar and D. D. Pathak, *Chem. Sci. Trans.*, 2014, **3**, 663.

37 A. R. M. Zarea, M. Rezaeib, M. Merajoddinb, H. Hamidianb, A. Zareb and M. K. Rostamic, *Sci. Iran.*, 2014, **21**, 2058.

38 H. Naeimi and Z. S. Nazifi, *J. Ind. Eng. Chem.*, 2014, **20**, 1049.

39 (*a*) B. P. Reddy, V. Vijayakumar, T. Narasimhamurthy, J. Suresh and P. L. Lakshman, *Acta Crystallogr., Sect. E: Struct. Rep. Online*, 2009, **65**, o916; (*b*) M. A. Bigdeli, G. H. Mahdavinia and V. Amani, *Acta Crystallogr., Sect. E: Struct. Rep. Online*, 2007, **E63**, o3493.

40 (*a*) M. M. Alam, R. Varala and V. Seema, *Mini-Rev. Org. Chem.*, 2023, **21**, 555; (*b*) M. Neetha, K. R. Rohit, S. Saranya and G. Anilkuma, *ChemistrySelect*, 2020, **5**, 1054.

41 M. L. da Silva, R. R. Teixeira, L. de Azevedo Santos, F. T. Martins and T. C. Ramalho, *Arab. J. Chem.*, 2020, **13**, 974.

42 A. N. Dadhania, V. K. Patel and D. K. Raval, *C. R. Chim.*, 2012, **15**, 383.

43 A. G. A. El-Helby, H. Sakr, I. H. Eissa, H. Abulkhair, A. A. Al-Karmalawy and K. El-Adl, *Arch. Pharm.*, 2019, **352**, 1900113.

44 (*a*) S. Limsuwan, E. N. Trip, K. Trhm, S. Piersma, A. Hiranrat, W. Mahabusarakam, S. P. Voravuthikunchai, J. M. V. Dijl and O. Kayser, *Phytomedicine*, 2009, **16**, 651; (*b*) M. Kaya, E. Demir and H. Bekci, *J. Enzyme Inhib. Med. Chem.*, 2012, **28**, 893.

45 (*a*) R. Sangwan, M. Saini, R. Verma, S. Kumar, M. Banerjee and S. Jain, *J. Mol. Struct.*, 2020, **1208**, 127786; (*b*) N. Mulakayala, P. V. N. S. Murthy, D. Rambabu, M. Aeluri, R. Adepu, G. R. Krishna, C. M. Reddy, K. R. S. Prasad, M. Chaitanya, C. S. Kumar and M. B. Rao, *Bioorg. Med. Chem. Lett.*, 2012, **22**, 2191; (*c*) F. Al-Omran, R. M. Mohareb and A. Abou El-Khair, *Med. Chem. Res.*, 2014, **23**, 1633.

46 G. Jones, P. Willett, R. C. Glen, A. R. Leach and R. Taylor, *J. Mol. Biol.*, 1997, **267**, 727.

47 G. M. Sheldrick, *Acta Crystallogr., Sect. A: Found. Adv.*, 2015, **71**, 8.

48 O. V. Dolomanov, L. J. Bourhis, R. J. Gildea, J. A. K. Howard and H. Puschmann, *J. Appl. Crystallogr.*, 2009, **42**, 341.

49 G. M. Sheldrick, *Acta Crystallogr., Sect. C: Struct. Chem.*, 2015, **71**, 8.

50 *Rigaku Oxford Diffraction*, CrysAlisPro Software System, 2022.

51 C. F. Macrae, I. Sovago, S. J. Cottrell, P. T. A. Galek, P. McCabe, E. Pidcock, M. Platings, G. P. Shields, J. S. Stevens, M. Towler and P. A. Wood, Mercury 4.0: from visualization to analysis, design and prediction, *J. Appl. Crystallogr.*, 2020, **53**, 235.

52 N. Aouf, *CCDC 2308384: Experimental Crystal Structure Determination*, 2023.

53 Y. Miyazaki, S. Matsunaga, J. Tang, Y. Maeda, M. Nakano, R. J. Philippe, M. Shibahara, W. Liu, H. Sato, L. Wangb and R. T. Nolteb, *Bioorganic Med. Chem. Lett.*, 2005, **15**, 2207.

54 S. Release, *2. LigPrep, Version 3.4*. Schrödinger, LLC, New York, NY, 2015, p. 26400175.

55 R. A. Friesner, J. L. Banks, R. B. Murphy, T. A. Halgren, J. J. Klicic, D. T. Mainz, M. P. Repasky, E. H. Knoll, D. E. Shaw, M. Shelley, J. K. Perry, P. Francis and P. S. Shenkin, *J. Med. Chem.*, 2004, **47**, 1749.

56 (*a*) E. C. Meng, T. D. Goddard, E. F. Pettersen, G. S. Couch, Z. J. Pearson, J. H. Morris and T. E. Ferrin, *Protein Sci.*, 2023, **32**, 4792; (*b*) E. F. Pettersen, T. D. Goddard, C. C. Huang, E. C. Meng, G. S. Couch, T. I. Croll, J. H. Morris and T. E. Ferrin, *Protein Sci.*, 2021, **30**, 82.

57 (*a*) E. Chow, C. A. Rendleman, J. K. Bowers, R. O. Dror, D. H. Hughes, J. Gullingsrud, F. D. Sacerdoti and D. E. Shaw, Desmond performance on a cluster of multicore processors, *DE Shaw Research Technical Report*,

New York, 2008, DESRES/TR-2008-01, https://deshawresearch.com/; (*b*) *Schrödinger Release 2023-4: Desmond Molecular Dynamics System, D. E. Shaw Research*, Maestro-Desmond Interoperability Tools, Schrödinger, New York, NY, 2023.

58 R. V. Krems, *Phys. Chem. Chem. Phys.*, 2019, **21**, 13410.

59 (*a*) A. D. Becke, *J. Chem. Phys.*, 1993, **98**, 5652; (*b*) M. M. Francl, W. J. Pietro, W. J. Hehre, J. S. Binkley, M. S. Gordon, D. J. DeFrees and J. A. Pople, *J. Chem. Phys.*, 1982, **77**, 3665.

60 M. J. Frisch, G. W. Trucks, H. B. Schlegel, G. E. Scuseria, M. A. Robb, J. R. Cheeseman, G. Scalmani, V. Barone, B. Mennucci and G. A. Petersson, *Gaussian-09 Revision A.02*, Gaussian Inc, Wallingford CT, 2009.

61 G. Zhang and C. B. Musgrave, *J. Phys. Chem. A*, 2007, **111**, 1561.

62 C. A. Lipinski, F. Lombardo, B. W. Dominy and P. J. Feeney, *Adv. Drug Delivery Rev.*, 2001, **64**, 17.

63 (*a*) A. Daina, O. Michielin and V. Zoete, *Sci. Rep.*, 2017, 7, 42717; (*b*) https://www.swissadme.ch/.

64 https://www.molsoft.com.